UNIVERSITÀ DEGLI STUDI DI PADOVA

Dipartimento di Fisica e Astronomia "Galileo Galilei"

Master Degree in Astrophysics and Cosmology

Final Dissertation

Search for exoplanets through pulsation timing of Delta Scuti stars

Thesis supervisor

Prof. Giampaolo Piotto

Thesis co-supervisor

Dr. Valerio Nascimbeni

Candidate

Valentina Vaulato

Academic Year 2020/2021

Alla mia nonna Lina
Ai miei genitori

« In principio Dio creò il cielo e la terra.
E la terra era informe e vuota
e le tenebre ricoprivano l'abisso.

...

E poi le stelle.
Dalla volta del cielo esse rischiarano la terra.
Dio le mise lassù per regolare
il giorno e la notte
e separare la luce dalle tenebre. »

Genesi, 1.

Table of Contents

Abstract 8
Sommario 10

1 Introduction **13**
1.1 Extrasolar Planets 13
1.1.1 Radial velocity technique 15
1.1.2 Transit detection method 16

2 Pulsating stars **21**
2.1 Physical mechanism 21
2.2 Delta Scuti stars and the Instability Strip 22
2.2.1 Observational history of Delta Scuti stars 23
2.3 The Pulsation Timing technique 25
2.3.1 Some results 28

3 TESS **32**
3.1 The TESS mission 32
3.1.1 Optical design 32
3.1.2 Observational strategy 33
3.1.3 TESS Input Catalog and Candidate Target List 34
3.1.4 Target Pixel File and Light curves 35

4 Target selection **37**
4.1 The Chang et al. (2013) catalog 37
4.2 Match with other catalogues 40
4.2.1 The final sample 41

5 Astrophysical parameters **46**
5.1 Empirical relations for the estimation of stellar masses 46

5.1.1 Chang 349, UZRet, V393 Car, V435 Car, HD 173844, GW Dra . . . 47
5.1.2 Chang 134 . . . 48

6 Harmonic analysis **52**
6.1 Common algorithm . . . 52
6.1.1 Light curve pre-conditioning and filtering . . . 52
6.1.2 The Lomb-Scargle Periodogram . . . 54
6.1.3 Harmonic fit: least-square approach . . . 56
6.1.4 Harmonic fit: refined MCMC model . . . 57
6.2 Algorithm applied to the three HADS . . . 60
6.2.1 Chang 134 . . . 60
6.2.2 V393 Car . . . 62
6.2.3 Chang 349 . . . 64
6.3 Computation of the expected LTE signal . . . 67
6.3.1 Chang 134 . . . 68
6.3.2 V393 Car . . . 70
6.3.3 Chang 349 . . . 71
6.3.4 General discussion . . . 73

7 Conclusions **75**
7.1 LTE fit of the (O-C) diagrams . . . 75
7.1.1 Chang 134 . . . 76
7.1.2 V393 Car . . . 78
7.1.3 Chang 349 . . . 80
7.2 TESS timing accuracy . . . 82
7.2.1 TESS absolute calibration . . . 86
7.3 Final discussion . . . 89
7.3.1 Outlooks . . . 90

Bibliography **93**

Abstract

The Pulsation Timing (PT) is a fruitful method to search and characterize exoplanets orbiting oscillating stars whose pulsation period, instrinsically very coherent, is phase-shifted because a perturbing companion induces the star to orbit around the barycenter of the system (so called Light Travel Effect or LTE). The more massive the perturber is, and the wider the star-perturber separation is, the larger will be the LTE signature. So far, only a handful of exoplanets have been discovered via such method compared to the 4,424 exoplanets already detected through other techniques.

My Master Thesis work consists in a pioneering analysis of short-cadence TESS light curves from a sample of suitable High Amplitude Delta Scuti variables (HADS, A0-F5) deriving, for the fundamental pulsation mode, phase shifts of the signal as a function of time (so called "$(O-C)$" diagram) to investigate if an LTE from an unseen companion can explain the behavior of the system.
For this purpose, HADS are the most appropriate pulsators to study since they exhibit short-period oscillations (1-3 hours) and high pulsation amplitudes (tenths of magnitudes) mostly in radial modes. In this favorable case, PT yields an high S/N, able to detect phase shifts of a fraction of second. I selected a shortlist of three HADS to investigate: Chang 134 (M = 1.38±0.03 $M_\odot$), V393 Car (M = 1.98±0.17 $M_\odot$) and Chang 349 (M = 1.78±0.16 $M_\odot$) whose masses are computed according to Moya et al., 2018 and Queiroz, Anders, Chiappini et al., 2020.
I carried out a two-level harmonic analysis exploiting the `VARTOOLS` Light Curve Analysis Program (Hartman and Bakos, 2016) by implementing an initial traditional least-squares regression and later a more sophisticated Monte Carlo Markov Chain approach to estimate error bars on phase shifts. From resulting values and associated uncertainties, computed individually for every one-orbit segment (∼2 weeks) of the light curve, I constructed the $(O-C)$ diagram to search for timing departures induced by LTEs. By fitting the $(O-C)$ diagram, I extracted the orbital period of the companion and the semi-amplitude of the LTE, "A". Thanks to the third Kepler's law, I computed the orbital semi-major axis "a" of the external body. Afterwards, assuming circular and edge-on orbits ($e = 0$, $i = \pi/2$), I estimated the mass of the companion, knowing both A and a. Lastly, I compared results obtained from my harmonic analysis with outcomes of the pilot study I set up to evaluate expected LTEs as a function of a for different perturbers.
I conclude that the $(O-C)$ diagrams I computed are consistent with the presence

of a brown dwarf companion (M $\simeq 49 \pm 5\ M_{\rm J}$) in orbit around Chang 134 at 0.4 AU and an M-dwarf binary (M $\simeq 195 \pm 18\ M_{\rm J}$) orbiting V393 Car in a 3-year orbit. On the contrary, the harmonic analysis of Chang 349 resulted to be not conclusive because no sinusoidal trend is able to model its $(O-C)$ diagram, and more data and temporal coverage is needed to draw definitive conclusions.

My analysis demonstrated the crucial role of the PT technique in characterizing orbital and intrinsic properties of companions orbiting at large separation from the host pulsating star. Being a less explored detection method, PT can be further developed in the near future offering significant contributions to the knowledge of evolved systems around pulsating stars. In the short term, the main source of photometric data will be the TESS mission which continues gathering data and extending the temporal baseline that will be complemented with other archival light curves or with on-purpose observations at ground-based facilities like the Asiago Observatory. Furthermore, my pioneering work on the PT technique can be generalized to a wider sample of pulsators, not only HADS or stars within the instability strip, by also addressing issues on the absolute calibration of TESS time stamps. To conclude, results obtained from the harmonic analysis I carried out in my master thesis project are fruitful for TESS past, present and future observations and they will turn out to be valuable and promising also for the forthcoming PLATO mission.

Sommario

Il Pulsation Timing (PT) è una tecnica utile per cercare e caratterizzare esopianeti orbitanti attorno a stelle oscillanti il cui periodo di pulsazione, intrinsecamente molto coerente, è sfasato perché un compagno perturbante induce la stella ad orbitare attorno al baricentro del sistema (cosiddetto Light Travel Effect o LTE). Più massiccio è il perturbatore e più ampia è la distanza stella-perturbatore, maggiore sarà il LTE. Finora, solo una manciata di esopianeti è stata scoperta con tale metodo rispetto ai 4,424 esopianeti già scoperti con altre tecniche.

Il mio lavoro di tesi magistrale consiste in un'analisi pionieristica di curve di luce TESS a breve cadenza da un campione di variabili Delta Scuti a grande ampiezza (cosiddette High Amplitude Delta Scuti, HADS, A0-F5) derivando, per il modo fondamentale di pulsazione, sfasamenti del segnale in funzione del tempo (il cosiddetto diagramma "$(O-C)$") per indagare se un LTE causato da un corpo secondario non visibile fotometricamente possa spiegare il comportamento fisico del sistema. A questo scopo, le stelle HADS sono i pulsatori più appropriati da studiare poiché mostrano oscillazioni di breve periodo (1-3 ore) e ampie ampiezze di pulsazione (decimi di magnitudine) per lo più in modi radiali. In questo caso favorevole, la tecnica del PT produce un S/N significativo, in grado di rilevare sfasamenti dell'ordine di una frazione di secondo. Ho selezionato una lista di tre HADS da studiare: Chang 134 (M = 1.38±0.03 $M_{\odot}$), V393 Car (M = 1.98±0.17 $M_{\odot}$) e Chang 349 (M = 1.78±0.16 $M_{\odot}$) le cui masse sono state calcolate secondo Moya et al., 2018 e Queiroz, Anders, Chiappini et al., 2020. Ho poi effettuato un'analisi armonica a due livelli sfruttando il programma `VARTOOLS` (Hartman and Bakos, 2016) e implementando inizialmente una regressione tradizionale dei minimi quadrati e successivamente un approccio più sofisticato, cosiddetto Monte Carlo Markov Chain, per stimare le barre di errore sugli sfasamenti. Dai valori risultanti e dalle incertezze associate, calcolati individualmente per ogni segmento orbitale ($\sim$2 settimane) della curva di luce, ho costruito il diagramma $(O-C)$ per cercare derive temporali indotte da LTEs. Fittando il diagramma $(O-C)$ ho estratto il periodo orbitale del compagno e la semiampiezza del LTE, "A". Grazie alla terza legge di Keplero ho calcolato il semiasse maggiore dell'orbita del corpo esterno "a". Successivamente, ipotizzando orbite circolari osservate di taglio ($e = 0$, $i = \pi/2$), ho stimato la massa del perturbatore, conoscendo sia A che a. Infine, ho confrontato i risultati ottenuti dall'analisi armonica con quelli di uno studio pilota che ho impostato per valutare il LTE atteso al variare di "a" e della la massa del

perturbatore. Ho trovato una nana bruna (M $\simeq 49 \pm 5\ M_{\rm J}$) in orbita attorno a Chang 134 a 0.4 AU e una nana M (M $\simeq 195 \pm 18\ M_{\rm J}$) orbitante attorno a V393 Car su un'orbita di 3 anni. Al contrario, l'analisi armonica di Chang 349 è risultata non conclusiva in quanto nessun andamento sinusoidale può modellare la distribuzione degli sfasamenti nel diagramma $(O - C)$.

La mia analisi ha dimostrato il ruolo cruciale della tecnica PT nel caratterizzare le proprietà orbitali e intrinseche di compagni esterni orbitanti a grande distanza dalla stella pulsante ospite. Essendo un metodo di ricerca esoplanetaria poco sfruttato, la tecnica PT può essere sviluppata nel prossimo futuro offrendo contributi significativi alla conoscenza di sistemi evoluti attorno a stelle pulsanti. La principale fonte di dati fotometrici sarà la missione TESS che continua a raccogliere dati ed estendere la baseline temporale che sarà ulteriormente integrata con altre curve di luce d'archivio o con osservazioni mirate da terra usando telescopi come l'Osservatorio di Asiago. Inoltre, il mio lavoro esplorativo sulla tecnica PT può essere generalizzato a un campione più ampio di pulsatori, non solo HADS o stelle all'interno della cosiddetta instability strip, affrontando anche questioni relative alla calibrazione assoluta dei time stamps del satellite TESS. In conclusione, i risultati ottenuti dall'analisi armonica che ho svolto nel mio progetto di tesi magistrale sono fruttuosi per le osservazioni passate, presenti e future di TESS e si riveleranno preziosi e promettenti anche per la futura missione PLATO.

Chapter 1
Introduction

1.1 Extrasolar Planets

Exoplanets (planets outside our Solar System) are defined according to the International Astronomical Union[1] (IAU) as:

- Objects having true masses below the limiting mass for thermonuclear fusion of deuterium[2] that orbit stars, brown dwarfs or stellar remnants and that have a mass ratio with the central object below the L4/L5 instability, i.e. $M/M_{central} < 0.04$, are "planet" (regardless of how they formed).
- The minimum mass and size required for an extrasolar object to be considered as a planet should be the same as that used in the Solar System.

The search for planets beyond our Solar System and their characterization became a relevant scientific object of interest since the early 1990s.
Beginner studies were published by Wolszczan and Frail, 1992, who discovered the first planetary system, and Mayor and Queloz, 1995 who discovered the first Jupiter-like exoplanets orbiting a Solar-type star. This discovery encouraged other scientists in the field which rapidly turned out to be avantgarde. So far, more than 4400 exoplanets have been confirmed[3] thanks to powerful technological developments in both ground-based and space-based missions.
Several techniques have been developed over the years (Perryman, 2018) for detecting exoplanets following a rapid technological progress:

- *Astrometry* measures the transverse component of the change of position of the host star induced by the gravitational influence of a perturbing external body. The observable astrometric signature, α, is the angular size of the semi-major axis of the stellar orbit about the barycenter as it appears projected

[1] https://www.iau.org
[2] Calculated to be $\simeq$ 13 Jupiter masses for objects of Solar metallicity.
[3] https://exoplanetarchive.ipac.caltech.edu

onto the sky-plane:

$$\alpha \simeq \frac{M_{\rm p}}{M_\star}\ a, \tag{1.1}$$

where a is the semi-major axis of the planetary orbit, $M_{\rm p}$ is the mass of the perturber and $M_\star$ is the stellar mass.

- *Microlensing* consists in variations of the observed flux of a magnified background star when a foreground star, the so called lens star, warps its wavefront according to laws of Einstein's general relativity. Eventually, the presence of a planetary system around the lens star is inferred by observing a distortion of the stellar light curve with respect to the predicted model for a single lens.

- *Imaging* concerns the direct observation of the planet as a resolved, point-like source of light. This light can be originated either by the planet itself as thermal emission or by the host star as reflected light. Since the planet-star angular separation is very small (usually $\ll 1$") the stellar emitted flux blinds the telescope when using conventional techniques, hiding the possible presence of a planet. For this reason, coronographs are the key to unveil the planet because they mask the star by stopping the stellar light.

- *Timing*: this is a general class of techniques where an astrophysical signal, which is supposed to be intrinsically periodic when no planets are present, is searched for any departure from a strict periodicity. This can be, for instance, the orbital period of already known planets in the same system (TTV; Transit time variations, Holman and Murray, 2005) or the orbital period of a binary star (ETV; eclipse timing variations). A particular scenario is the case of planets orbiting variable pulsating stars. These exoplanets can be detected by finding a modulation of the pulsation period that can be modeled as a light-travel effect (LTE) due to the star oscillating around the common barycenter of the planet-star system combined with the finite speed of light. The pulsation timing method is the one employed in this work and for such reason is explained in much more detail in section 2.3.

However, the most commonly used detection techniques are the radial velocity and the transit method explained in more detail in the following subsections. Those are also the most fruitful techniques so far, in terms of discovered exoplanets as shown in the histogram below (Fig. 1.1).

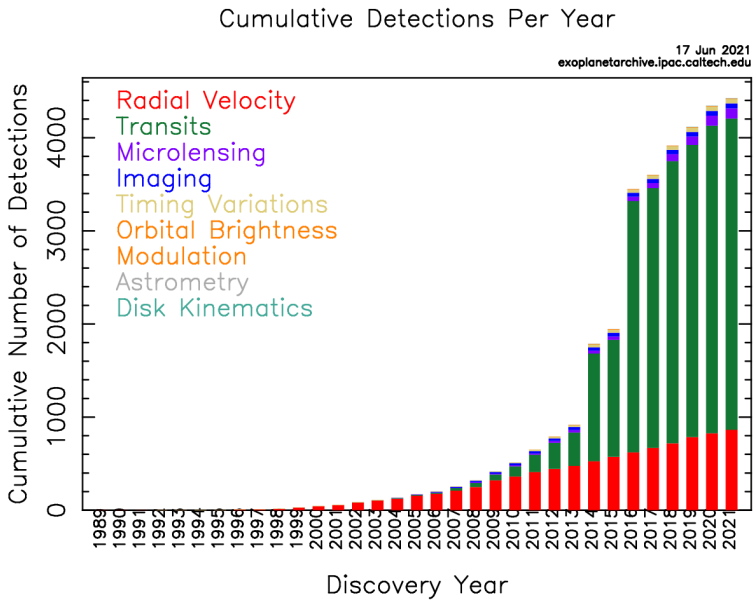

Figure 1.1: Histogram illustrating the number of detections per year. Colors represent detection techniques exploited. Transits (in green) and radial velocities (in red) are the most used detection techniques since 1999. Last update: 17 June, 2021. Image credit: https://exoplanetarchive.ipac.caltech.edu.

1.1.1 Radial velocity technique

When a star is orbited by a secondary body, the gravitational interaction induces a stellar motion around the common barycenter of the system. Consequently, the star periodically moves along the line of sight of a distant observer and spectroscopic observations will highlight this motion as a Doppler shift of the stellar spectral absorption lines. By modeling this signal and measuring the stellar radial velocity (RV) semi-amplitude (Perryman, 2018)

$$K_{\rm star} = (1-e^2)^{-1/2} \frac{M_{\rm p,min}}{(M_\star + M_{\rm p,true})^{2/3}} \left(\frac{P_{\rm orb}}{2\pi G}\right)^{-1/3}, \tag{1.2}$$

it is possible to derive the orbital period and the minimum mass of the perturber ($M_{\rm p,\ min} = M_{\rm p,\ true}\ \sin(i)$, where i is the inclination of the orbital plane with respect to the sky plane, see figure 1.4). In the figure below (Fig. 1.2) is reported an example of the typical radial velocity curve of a planet-hosting star, folded over the orbital period of the planet.

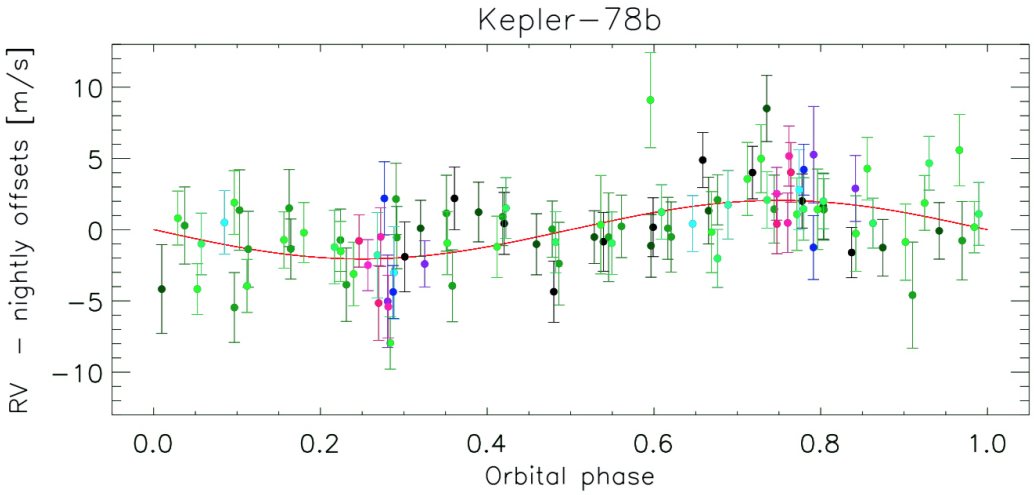

Figure 1.2: RV curve of the Ultra Short Period (USP) exoplanet Kepler-78b corrected by the offset induced by the stellar activity as a function of the orbital phase. Each color represents a different night of observation gathered by HARPS-N. The red curve is the best-fit model returning an estimated planetary mass of $M_{\rm p} = 1.9 \pm 0.3\ M_{\oplus}$.
Image credit: Vaulato and Gandolfi, 2019.

The first convincing exoplanetary detection via RV method dates back to the pioneering publication of Mayor and Queloz, 1995 who discovered the first hot Jupiter, 51 Peg b, orbiting an host star similar to our Sun.

The RV method is often applied in combination with other detection techniques (such as the transit method) as part of the so called "follow-up" analysis for the confirmation and better characterization of the planetary system. Furthermore, RV curve might be warped by the so called Rossiter-McLaughlin (RM, Rossiter, 1924 and McLaughlin, 1924) effect which occurs in eclipsing systems when the companion crosses in front of a rotating star (i.e. transits) thus creating a distortion in the shape of the stellar RV curve. Modeling the RM effect, astronomers are able to estimate the sky-projected spin-orbit angle between the planet's orbital plane and the host star equatorial plane.

1.1.2 Transit detection method

A transit is an event occurring when the inclination "i" of the orbital plane of a planet with respect to the line of sight of the observer is close to 90 degrees (see Fig. 1.4). Indeed, when the planet transits in front of the star, the stellar light

curve exhibits a temporary dimming which lasts until the secondary body does not overlap its host star anymore. Such a dimming can be detected by gathering high-precision photometric time series of the host star ("light curve") and by modeling its shape we can measure the radius, orbital inclination and orbital period of the transiting planet.
In first approximation, the transit depth is given by:

$$\Delta F \simeq \left(\frac{R_\mathrm{p}}{R_\star}\right)^2, \tag{1.3}$$

where R_p and $R_\star$ are the planetary and stellar radius, respectively.
The figure below (Fig. 1.3) shows a typical stellar light curve affected by a transit feature.

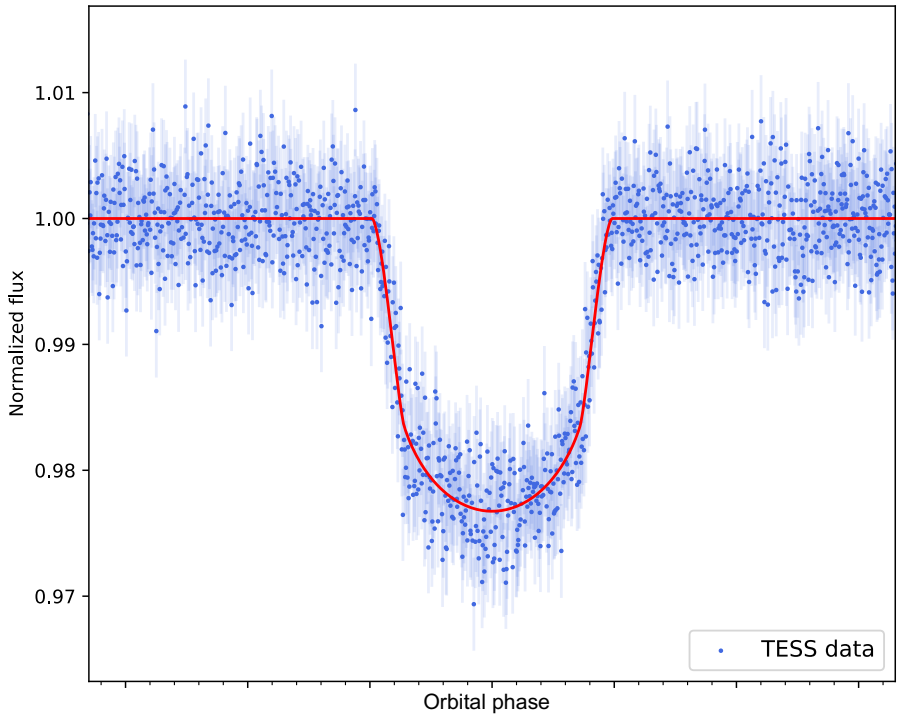

Figure 1.3: Transit signature of HAT-P-12b. The normalized stellar flux (TESS data) is plotted as a function of the orbital phase and is fitted by the transit model (red line; own work).

The first exoplanet detected through the transit technique (Henry et al., 2000) was a gas giant orbiting the star HD 209458 (HD 209458 b), previously discovered by RVs.

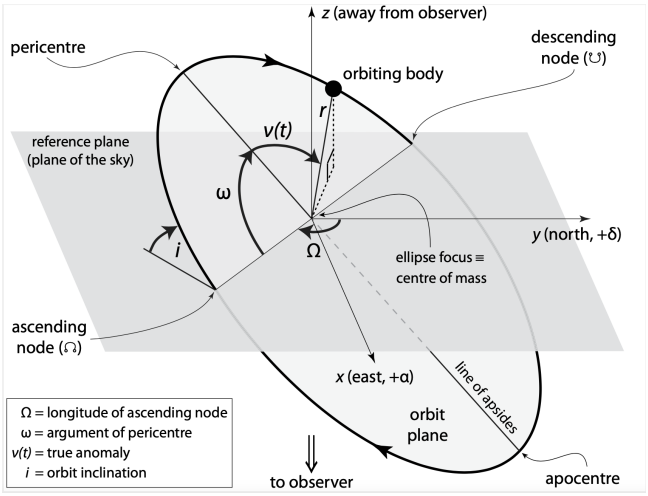

Figure 1.4: Geometry of an elliptical orbit in three dimensions where the reference plane is tangent to the celestial sphere.
Image credit: Perryman, 2018.

As ultimate goal, from the combination of RV and transit detection methods, astronomers are able to measure or at least constrain the planetary bulk properties, i.e. true mass, radius and density. If the planetary mass and radius are known, the chemical composition, mean density and inner structure of the planet are outlined by constructing the so called mass-radius diagram (e.g. Fig. 1.5). The reported graph shows curves of composition, so called iso-chemical composition curves, considering elements like water, silicates and iron. These curves trace the potential chemical structure of the planet depending on its radius and mass. Indeed, in the central region of the diagram astronomers expect to find dense terrestrial planets (i.e. Earth twins and/or Super-Earths), composed mainly by rocks, metals, silicates and a thin captured gaseous atmosphere. Quite the opposite, for higher masses and radii (e.g. Jupiter radius $R \simeq 11.2\ R_{\oplus}$ and mass $M \simeq 317.8\ M_{\oplus}$) astronomers find gas giant planets, mostly made of hydrogen and helium (~ 90 % of the total mass) with a core of silicates and iron.

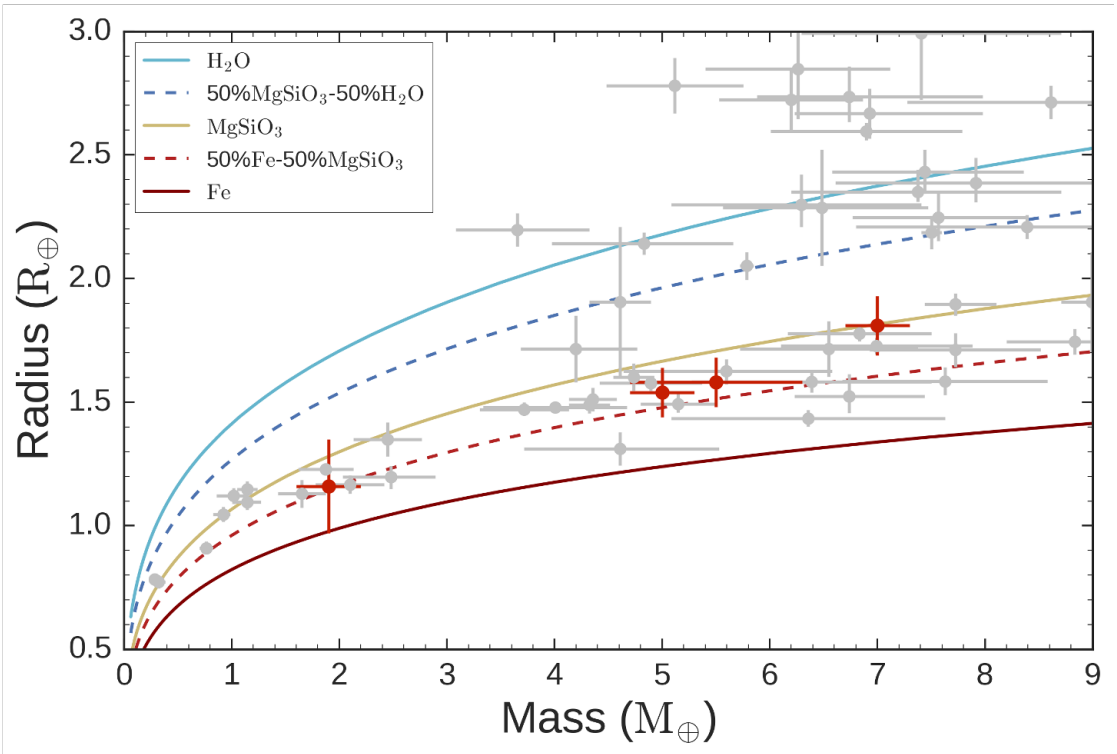

Figure 1.5: Mass-Radius diagram in Earth units. The blue, red and yellow solid curves indicate a composition made of water, iron and bridgmanite, respectively. The dashed curves indicate hybrid chemical compositions. Gray dots with uncertainties represent a general distribution of exoplanets whereas the red dots with respective error bars are four Earth-like exoplanets; from left to right: Kepler-78b, K2-141b, CoRoT-7b and K2-131b.
Image credit: Vaulato and Gandolfi, 2019.

Chapter 2
Pulsating stars

2.1 Physical mechanism

Asteroseismology is a powerful method for investigating the inner structure of stars by studying their modes of oscillation. A particular class of stars for which pulsations are easy to detect are the so called "Delta Scuti" (δSct, from the name of its prototype) on which this thesis is focused. The classical mechanism which drives the pulsation is the so called "heat-engine" mechanism, for the first time proposed by Eddington, 1917 for Cepheid variables. It strictly depends on the change of the stellar opacity, K. The K-variation is caused by the heating of a He-rich stellar atmospheric layer which expands, becomes more ionized and, as a consequence, more opaque. The transparency drop of such atmospheric layer partially blocks the outgoing stellar flux which appears dimmer to the observer. The trapped radiation will heat up more the helium layer that continues to expand and ionize. While the layer is expanding, the temperature starts decreasing and the helium layer becomes less opaque, such that the stellar flux is able to "escape" that atmospheric level reaching the observer. The escaped light does not heat up the atmosphere anymore and the helium component cools down, contracting. δSct, together with other pulsators like RR Lyrae variables and rapidly oscillating Ap stars (roAp), are typical A stars driven by the Eddington mechanism.
For completeness, as presented by Guzik et al., 2000, I mention that there is another process responsible of stellar pulsations for those kind of stars: the convective-flux modulation mechanism operating in particular in the case of γ Doradus variables if they have sufficiently deep envelope convection zones.
Pulsators are described by pulsation modes which refers to three main quantum numbers:

- **n** : overtone or radial order, it expresses the amount of radial nodes;
- **l** : degree, it indicates the number of surface nodes;
- **m** : azimuthal order, its absolute value specifies the number of surface nodes which are lines of longitude. If $|m| < 0$ the modes are prograde and frequencies higher in the observer's reference frame, viceversa the modes are

retrograde.

Gravity and pressure are the two main restoring forces for stellar oscillations that act bringing the star back to its equilibrium state. Therefore, exist pressure modes (**p**) having $n > 0$ and gravity modes (**g**) having $n < 0$ and $l \geq 1$, since they are non-radial modes. In the case of radial motion, the gravitational force increases during compression and gravity accelerates the oscillations instead of restoring them hence, in this configuration, the pressure acts as a restoring force. On the contrary, in case of transverse motion, gravity restores the motion via buoyancy (Handler, 2013).

2.2 Delta Scuti stars and the Instability Strip

The Instability Strip is a portion of the Hertzsprung–Russell diagram enclosing the vast majority of known pulsating stars. It is interest of this work to focus on δSct variables.
δSct, as described by Kurtz, 2000, pulsate in both radial and non-radial modes, have H-core-burning and may be both post- and pre- main sequence stars, ranging between spectral types A2V to F0V and A3III to F5III. Referring to the review of S. Murphy, 2015, their observational instability strip can be "vertically" split in two regions:

1. δSct nearby the Zero Age Main Sequence (ZAMS) have effective temperatures in the range $7380 < T_{\text{eff}} < 8600$ K, a roughly surface gravity of $\log(g) \approx 4.30$ in cgs units and masses between $1.2 < M < 2\ M_{\odot}$;
2. δSct at the top of the instability strip (further from the ZAMS) have $6300 < T_{\text{eff}} < 7530$ K and $\log(g) = 3.25$.

The δSct instability strip is delimited by the red and blue edges which are theoretically extimated for non-radial pulsating δSct by Dupret et al., 2004 through the Time-Dependent Convection (TDC) approach based on the work of Gabriel et al., 1975. TDC models are computed for several values of the free mixing-length parameter (α) that expresses the efficiency of the convection acting in combination with the pressure scale height in the stellar interior (Canuto, 1990). Graphically, the results are summarized in Fig. 2.1.

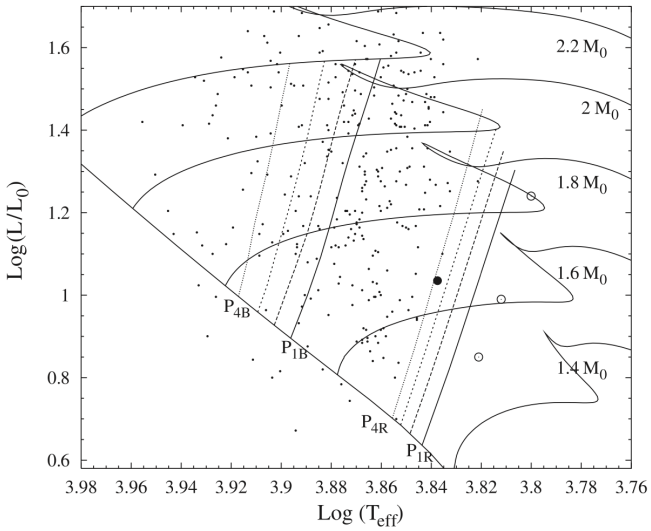

Figure 2.1: δSct distribution in logarithmic scale within the instability strip, mostly above the ZAMS. Blue and red edges are theoretically derived for $\alpha = 1.8$, best-fit value for ground-based observations. Curves are the evolutionary tracks, i.e. isochrones, computed for different stellar masses: from the Chandraseckhar mass, 1.4 $M_{\odot}$, to 2.2 $M_{\odot}$, in steps of 0.2 $M_{\odot}$. Image credit: Dupret et al., 2004.

The diagram above (Fig. 2.1) is sensitive to the metallicity parameter, Z. Indeed, lower values of Z will shift the evolutionary tracks to higher $T_{\rm eff}$ and higher $\log(g)$. According to the Stefan-Boltzmann law ($L \propto R^2T^4$), metal-poor stars having same age and mass are more luminous; this assumption will affect the stellar lifetime along the main sequence since the core hydrogen will exhaust more quickly with respect to metal-rich stars. Therefore, evolutionary tracks change according to the stellar metal abundance. On the other hand, Z does not influence the position of the edges limiting the instability strip because for δSct the HeII driving zone is only partially ionised (Balona, 2014).

2.2.1 Observational history of Delta Scuti stars

Before the advent of space-based telescopes such as Kepler mission (Borucki et al., 2010), CoRoT (Moutou et al., 2013) and, later on, TESS (Ricker et al., 2014), ground-based observations were mostly limited to a photometric precision of about 1 mmag (thousandth of magnitude). Astronomers believed that, by improving the photometric precision and lowering the detection limits, the frequency spectra of δSct would have resulted much more complex than what was previously thought. The first Kepler observations were able to reach detection limits down to 1-10

μmag, confirming the already predicted spectral complexity of variable stars.
Before the advent of space-based photometry, the best known δSct were the so called High Amplitude Delta Scuti (HADS), now estimated to be merely the $\sim$ 0.24% of the stars in the instability strip (Lee et al., 2008). Indeed, there was no need of high precision photometry in order to detect such targets. HADS were associated to slow-rotating pulsators (rotational speed nowadays extimated to be $\simeq$ 160 Km$\cdot$s^{-1}, S. Murphy, 2015) favoured in radial oscillating modes and located in the centre of the instability strip.
Thanks to the pioneering space-based observations, HADS are defined as a small subgroup of δSct stars whose peak-to-peak light variation is greater than 0.3 mag (S. Murphy, 2015). HADS have the highest amplitudes making them the best suitable targets for investigating the evolution of frequency and period modulation when a long baseline of observations is available. They are a few because the vast majority of the δSct population is composed by low-amplitudes ($\sim$ 1 mmag, achievable thanks to innovative space-based photometry) and non-radial modes.

Below (Fig. 2.2 and 2.3), I reported two examples (from TESS short-cadence photometry) of typical light curves of one "classical" δSct pulsator, GW Dra (top panel) and of one HADS, Chang 349 (bottom panel).

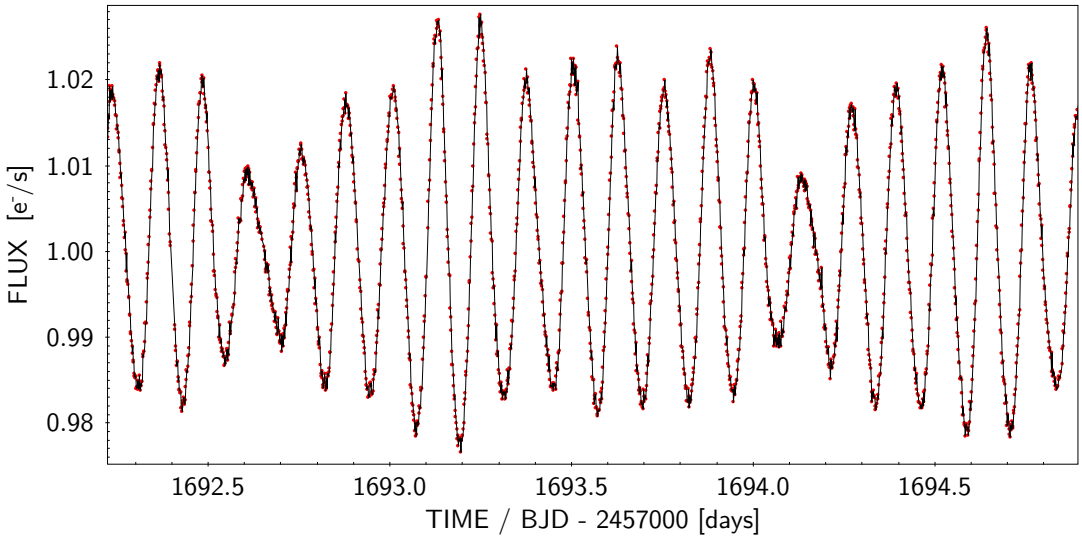

Figure 2.2: Normalized light curve (TESS sector 1) of δSct pulsator GW Dra. Flux in electrons per second as a function of the barycentric time.

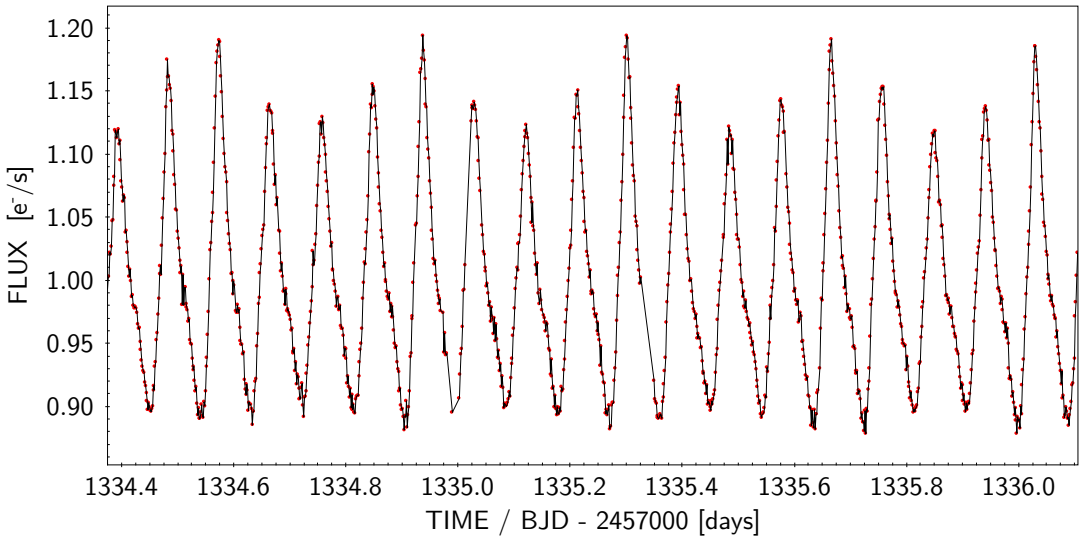

Figure 2.3: Normalized light curve (TESS sector 1) of the HADS pulsator Chang 349. Flux in electrons per second as a function of the barycentric time.

2.3 The Pulsation Timing technique

Pulsation timing (PT, Hermes, 2018) is a kinematical technique for the detection of exoplanets orbiting periodically variable stars. Indeed, variables such as δSct or pulsars[1] are highly regular pulsators and can be thought as precise astrophysical clocks. When orbited by an external (or more than one) body(ies), the primary star oscillates around the barycenter of the system. Since the speed of light is finite, the component of the orbital motion along the line of sight breaks the strong periodicity of the stellar pulsations because of what is known as light-travel effect (LTE). Therefore, any time delay affecting the incoming stellar signal could be seen as a hint of the presence of one or more additional bodies gravitationally bound to the variable star. If the measurement errors are small enough, the LTE technique could be in principle sensitive to perturbers down to the planetary regime. To be sure that the observed time delay is actually due to an LTE effect, the different pulsation modes can be individually investigated, since a purely kinematic effect is supposed to be coherent in time and to identically affect all the pulsation modes of the signal.
The semi-amplitude of the LTE, considering a perturber on a circular orbit (that

[1]Pulsars (Perryman, 2018, chapter 4) are highly spinning, magnetized and rapidly rotating neutron stars, resulting from the collapse of massive stars (typically ranging between $\sim$8 to 40 $M_{\odot}$). Millisecond pulsars are a peculiar subgroup since are low-magnetized and extremely regular pulsators with period variations at a rate of $\sim 10^{-19}$ (Bailes, 1996).

is having a null eccentricity, $e = 0$) around the host star, is:

$$A \simeq \frac{a \sin(i)}{c} \frac{m_{\rm p}}{M_\star} \ , \tag{2.1}$$

where c is the speed of light, a is the orbital semi-major axis, i is the inclination of the orbital plane with respect to the sky plane, m_p is the mass of the perturber and $M_\star$ is the stellar mass under the simplifying assumption that $M_\star \gg m_{\rm p}$. Observationally, the LTE translates in a phase shift of the oscillations which is in principle detectable through Fourier analysis.
The scenario described above is the simplest one. For a more complete description a Fourier harmonic analysis is needed. Following this approach, the light-travel-time delays can be analytically translated into a Fourier series of sinusoidal functions (Hermes, 2018):

$$\tau(t) = \sum_{k=1}^{N} A_k \sin\left(\frac{2\pi k t}{P_{\rm orb}} + \phi_k\right), \tag{2.2}$$

where A_k is the semi-amplitude of the signal, $P_{\rm orb}$ is the orbital period and ϕ_k is the phase referred to a zero-time point.
Equation (2.2) is the base for the construction of the so called "periodogram" (Zechmeister and Kürster, 2018) from which the most prominent peak, corresponding to the dominant period, is extracted.
A common tool in this search is the so called "$(O-C)$" diagram, where the observed phase of a given pulsation mode (O, "observed") is compared to the theoretically computed values (C, "calculated") for a coherent pulsation period corresponding to the dominant peak of the average periodogram. Searching exoplanetary signatures, it is necessary to investigate the $(O - C)$ diagram for as many pulsation modes as possible since, if the perturber were a planet, it is supposed to alter equally the arrival times of all pulsation modes .
Residuals can be mathematically written as (Hermes, 2018, taking the cue from Kepler et al., 1991):

$$O - C = t_0 + \Delta P E + \frac{1}{2} P \dot{P} E^2 + A_1 \sin\left(\frac{2\pi E}{P_{\rm orb,1}} + \phi_1\right), \tag{2.3}$$

where t_0 is the reference phase, ΔP is the uncertainty in the pulsation period, $\dot{P}$ is the period change in time, ϕ_1 is the phase-variation phase and A_1 is the amplitude of the phase variations due to an external body perturbing the system. E is the number of epochs calculated as the integer ratio $E = t/P$, observed times t divided by the pulsation period P.
Graphically, the $(O-C)$ diagram for a circular orbit is similar to its radial velocity curve, having a sinusoidal shape as shown in Fig. 2.4, extrapolated from the work of Mullally et al., 2009.

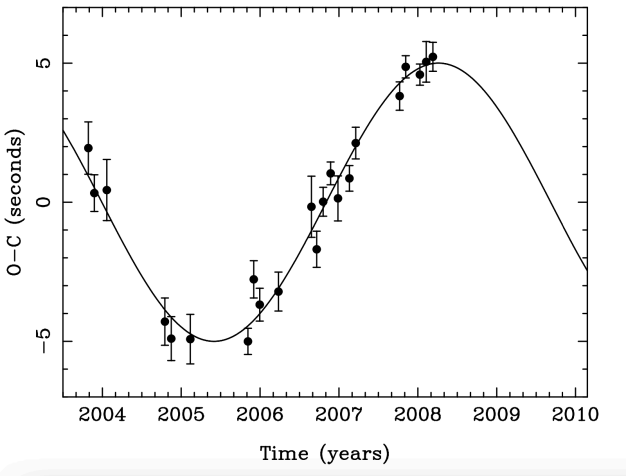

Figure 2.4: Example of the expected $(O - C)$ diagram in the pulsation timing analysis. The figure extracted from Mullally et al., 2009 represents the residuals in pulse arrival time of the white dwarf GD 66 perturbed by a 2 M_J exoplanet in a 4.5 year orbit.

In the more general case of eccentric orbits, according to the work of Irwin, 1952, the shape of the LTE curve is similar to a RV curve having half the eccentricity and ω decreased by 90 degrees, where ω is the angle indicated in Fig. 2.5. This approximation is accurate only for small eccentricities.

Based on what I described in the previous sections, in order to optimally exploit the PT technique to search for planetary-mass objects orbiting δSct stars, I need:

- A photometric time series ("light curve") spanning a temporal baseline long enough to sample the orbital period of the perturber. The wider the observational baseline is, the greater will be the sensitivity of PT to larger semi-major axes and therefore to smaller planetary masses (according to equation 2.1);
- A signal-to-noise ratio (S/N) high enough to constrain the phase shift of the oscillations to a level comparable with the LTE amplitude computed by equation 2.1. For a given instrument and target magnitude, this is more easily achieved by observing targets showing short-period, high-amplitude and single-mode pulsations (for example HADS, analyzed in this work).

Firstly the Kepler mission (Borucki et al., 2010) and afterwards the TESS mission (Ricker et al., 2014) proved to be excellent instruments for providing a large number of high-precision light curves over a very wide field of view. The present

thesis work made use of a small subset of TESS light curves; the general design and observing strategy of TESS will be presented in Chapter 3.

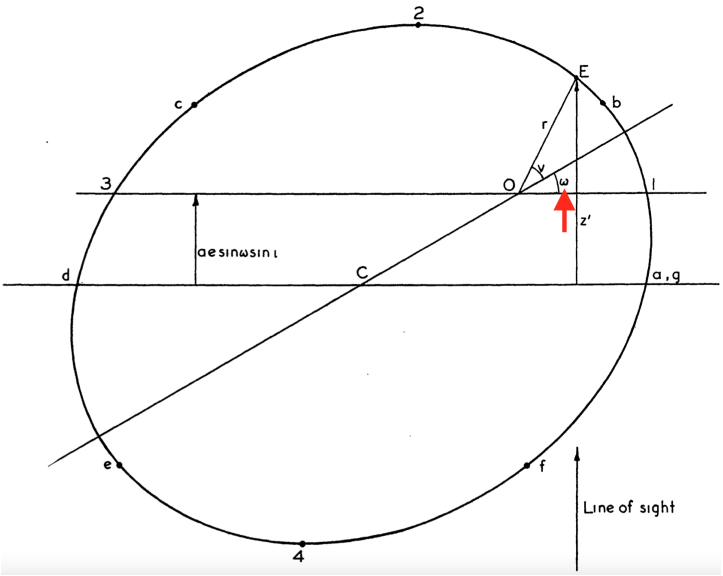

Figure 2.5: In this model E is the orbital position of the secondary component of an eclipsing binary system, as investigated by John B. Irwin in its review. The segment dCa is the intersection between the orbital plane and the tangent plane passing through the center of mass. In this frame the inclination angle, i, is assumed to be 90 degrees. Adapted from: Irwin, 1952.

2.3.1 Some results

Compared to transits or radial velocities, the PT is a niche method to detect exoplanets because only high-mass perturbers are detectable with the current technology with a sufficient degree of accuracy. Indeed, the majority of LTE perturbers discovered orbiting pulsating stars are in fact stellar-mass companions. During the Kepler mission (Borucki et al., 2010) many stellar binaries have been discovered orbiting δSct stars, later on confirmed by spectroscopic radial velocities follow-up (S. J. Murphy, Shibahashi and Bedding, 2016, a).
So far, only a handful of exoplanets orbiting δSct have been discovered. One of the most relevant result was achieved by S. J. Murphy, Bedding and Shibahashi, 2016 (b) who investigated a Kepler photometric time series. Thanks to the PT technique, they detected for the first time a Jupiter-mass exoplanet orbiting a main sequence A star in or near the habitable zone. The host star, KIC 7917485, is a metal-poor δSct with mass $M_\star \simeq 1.63\ M_\odot$ typical of the instability strip kind of objects. The time delays affecting the most prominent frequency-peaks result

in a phase modulation of 7.1 ± 0.5 s, consistent with a planet having minimum mass ≃ 11.8 M_J (close to the brown dwarf-planet boundary) and orbital period ≃ 840 days.

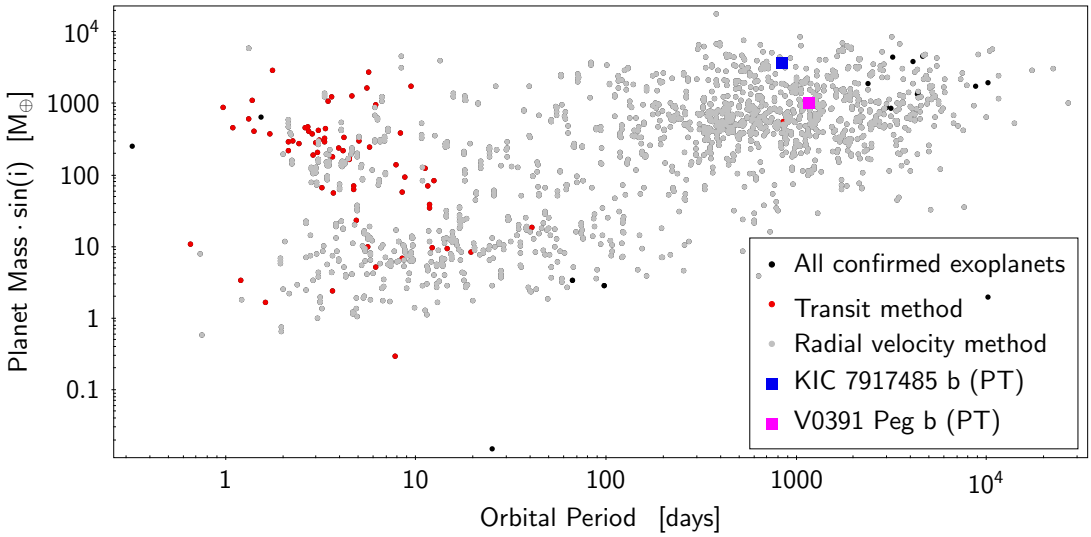

Figure 2.6: Planetary minimum mass vs Orbital Period of all confirmed exoplanets. In black all exoplanets discovered for which orbital period and minimum mass are known. In red and gray exoplanets discovered through transit method and radial velocity technique, respectively. The blue and pink squares show the only two exoplanets discovered via PT technique. In particular, KIC 7917485 b is the first exoplanet discovered via PT method in orbit around a δSct star. As it is clearly evident, planets discovered through PT are just a tiny subgroup, especially compared with exoplanets detected thanks to radial velocity and transit methods. Data credit: https://exoplanetarchive.ipac.caltech.edu.

V0391 Peg b (Silvotti et al., 2007) is a giant exoplanet in orbit around the hot subdwarf B star V0391 Peg having short-period and p-mode pulsations. Planetary properties are derived thanks to multiple observations carried out by several observatories. Its minimum mass and orbital period are ≃ 3.2 M_J and ≃ 1170 days, respectively. Obtained planet's properties are compatible with a phase modulation of 5.3 ± 0.6 s. Both KIC 7917485 b and V0391 Peg b are massive exoplanets orbiting at a wide separation from their host star. The more massive the perturber is and the broader the star-perturber separation is, the larger will be the LTE signature. Indeed, the challenge behind PT technique is to discover smaller exoplanets (optimistically down to Earth size and mass) in orbit nearby their stars, since they would induce low-amplitude LTEs. For this purpose, a key to improve

the sensitivity of the PT method is to avoid TESS systematic errors by calibrating accurately its timestamps (details discussed in section 7.2).

Chapter 3
TESS

In this chapter I review the technical and scientific characteristics of the Transiting Exoplanet Survey Satellite (TESS), whose light curves have been analyzed in this work.

3.1 The TESS mission

The Transiting Exoplanet Survey Satellite (TESS, Ricker et al., 2014) is a NASA mission launched on April 18th, 2018 aboard a SpaceX Falcon 9 rocket. The highly-elliptical stable orbit of TESS around the Earth has an orbital period of approximately 13.7 days, kept in a 2:1 resonance with the Moon; in such a way, the gravitational perturbations due to our satellite are negligible because the Moon is always beforehand or delayed of 90 degrees at apogee with respect to TESS.
TESS is devised for searching Super Earth- and Neptune- like exoplanets transiting bright and nearby main-sequence dwarfs having spectral type F5 to M5. Thanks to the TESS detector band pass, very extended in the "red" tail (up to 1 μm), K and M dwarfs are particularly suited as targets. As a consequence of the much wider field of view (encompassing nearly the whole sky at the end of the nominal mission) stars targeted by TESS are much more brighter on average with respect to those observed by the Kepler mission (Borucki et al., 2010). This is of course a great advantage especially when it comes to the follow-up of candidate planets, since spectrographs require a large number of photons to carry out ultra-precise observations.

3.1.1 Optical design

TESS is equipped with four identical cameras supplied with four $f/1.4$ lenses having a lens hood each to mitigate the impact from light scattered by the Earth and the Moon. Each camera covers a wide field of view (FOV) of 24° x 24° and has an effective diameter size $D \sim 10$ cm, optimized for high-precision photometry needed in order to detect transits by small planets. To the same aim, fast temporal cadence is required: light curves are gathered for a selected sample of stars

at a 2-minute cadence (2 sec-exposure images summed up into consecutive groups of 60), whereas Full Frame Images (FFIs) are produced and downloaded on Earth every 30 minutes of exposure time.
The focal plane of each camera is made of an array of four back-illuminated MIT/Lincoln Lab CCID-80 devices with 4096 x 4096 pixels covering a region of 62 x 62 mm^2. Each CCID-80 forms an imaging area of 2048 x 2048 pixels. In order to reduce the impact of the dark current noise, the CCD assembly must operate at a temperature of -75 Celsius degrees.
TESS detector band pass spans a broad red-optical wavelength range from 600 nm to 1000 nm, chosen to reduce photon-counting noise and to increase the sensitivity of the cameras for the detection of small transiting exoplanets in orbit around red and cool dwarf stars, especially K and M dwarfs. The blue cutoff at 400 nm is due to practical optical design reasons.

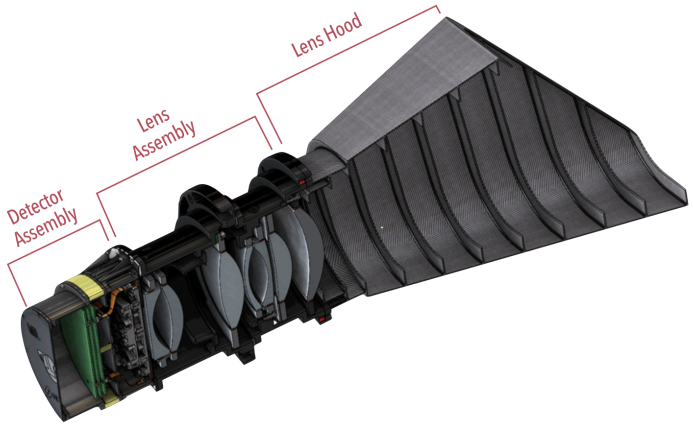

Figure 3.1: TESS wide FOV CCD Camera: 105 mm aperture and 24° x 24° FOV. Image credit:https://heasarc.gsfc.nasa.gov/docs/tess/

3.1.2 Observational strategy

The TESS observational strategy is based on so called "sectors", four-week pointings staring at the anti-solar direction, eventually mapping a whole ecliptic hemisphere in one year, after 13 sectors. The southern and northern ecliptic hemispheres were mapped during Year 1 and Year 2 of the mission[1], respectively, just avoiding only a small 12-degree strip across the Ecliptic. During the Year 3 of the mission, from July 2020 until July 2021, the southern hemisphere is being observed again. During the future Year 4 of the mission (July 2021-September 2022) the northern ecliptic hemisphere will be partially re-observed, together with 240° of

[1]Year 1 from July 2018 to July 2019, Year 2 from July 2019 to July 2020.

the ecliptic never spanned before.
Each of the 36 sectors already covered by TESS is observed for at least 27 days, corresponding to two orbits of the satellite around the Earth. The maximum coverage of a sector can be 351 days close to the ecliptic poles down to a minimum of 27 days at low ecliptic latitudes. The forthcoming James Webb Space Telescope (JWST, Gardner et al., 2006) will scan in greater details that area, labeled JWST continuous viewing zone (CVZ), for a better characterization of the targets in those sectors, providing much more informations useful for a follow-up spectroscopic investigation. During the observation epoch, the only interruption happens when data are downloaded after each orbit.

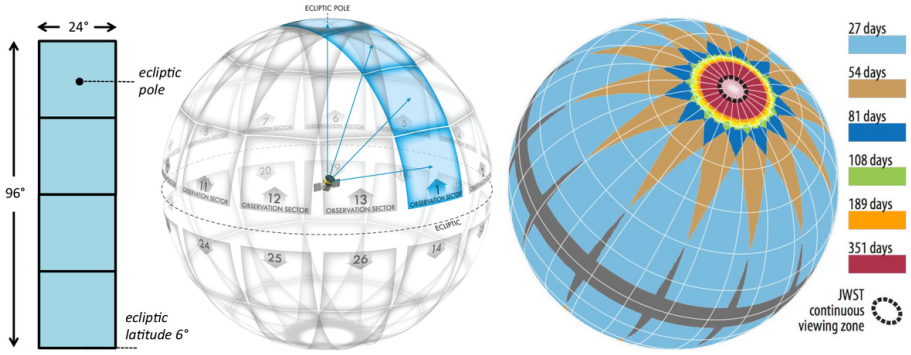

Figure 3.2: Left: Combined FOV of four TESS cameras. Middle: Sector-based coverage of TESS from the ecliptic plane to the ecliptic pole onto the celestial sphere. Right: Schematic illustration of the time coverage of different regions of the sky surveyed by TESS onto the celestial sphere. The dashed circle is the area which will be ontinuously observed by the forthcoming JWST.
Image credit: Ricker et al., 2014.

3.1.3 TESS Input Catalog and Candidate Target List

The TESS Input Catalog (TIC, Stassun et al., 2019) is a list of suitable targets which can be observed by the mission aiming to look for transit signatures in their flux light curve. These sources have to be carefully selected not only according to their stellar parameters, but also minimizing the presence of background and/or foreground contaminating sources that may lie within the same photometric aperture mask. This is a crucial issue with TESS since the sky-area projected onto a pixel covers about 21 x 21 arcsec^2 and the Point Spread Function (PSF) is extended for about 1-2 pixels.
In this work I used the TIC-8 version based on Gaia Data Release 2 (Gaia DR2)

photometric catalog, including roughly 1.5 billion stars. According to Stassun et al., 2019, in order to preserve the continuity with the previous TIC version (TIC-7) which used the 2MASS photometric catalog as a base point-source, the obsolete TIC-7 sources are translated into the new TIC-8 catalog thanks to associations between 2MASS and Gaia DR2 already provided by Gaia DR2. The TIC can be found in the Mikulsky Archive for Space Telescopes (MAST)[2].
A subset of TIC is the Candidate Target List (CTL). The CTL contains all those high-priority targets which are the most promising hosts of transiting exoplanets. It includes all TIC targets brighter than 13 TESS magnitudes, with radius smaller than 5 $R_{\odot}$ and all stars in the Cool Dwarf Catalog (CDC). CTL counts ∼9.5 million stars. From the CTL, which is a prioritized list, the actual targets to be observed in short-cadence mode are chosen on a sector-by-sector basis.

3.1.4 Target Pixel File and Light curves

The Target Pixel Files (TPFs) are cut-out images (in FITS file format) of an observed source coming from pixels limited within a set up photometric aperture mask. These pixels provide data that build the target light curve, namely stellar flux time series produced in short-cadence (every 2 minutes) using Simple Aperture Photometry (SAP). In this work, I preferred to use Pre-Search Data Conditioning Simple Aperture Photometry (PDCSAP) because stellar light curves are cleaner with respect to SAP series since systematic long term trends are removed.

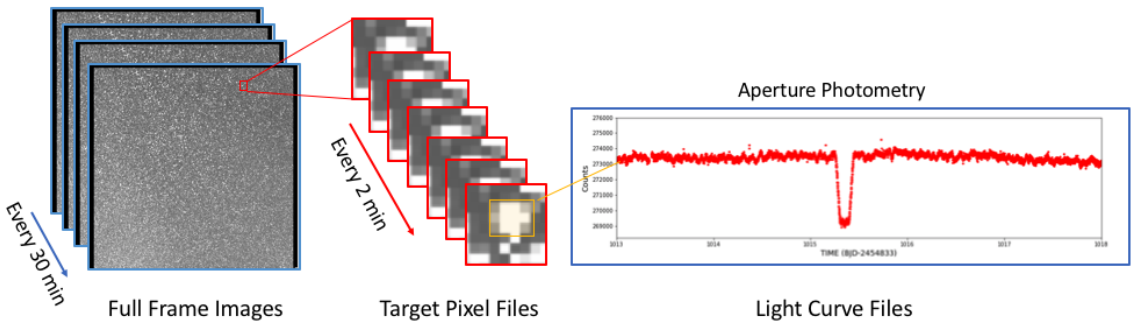

Figure 3.3: TESS photometric data products. Image credit: https://heasarc.gsfc.nasa.gov/docs/tess/data-products.html

[2] https://archive.stsci.edu/tess/

Chapter 4
Target selection

For this thesis work at first I selected an initial input list of suitable stellar targets whose extracted TESS light curves have been investigated. δSct stars are the objects of interest for this thesis: the reference catalog chosen as starting point is that published by Chang et al., 2013, consisting in a list of 1,578 δSct. In the following sections I will describe the details and the criteria of the target selection process.

4.1 The Chang et al. (2013) catalog

Seo-Won Chang and collaborators (Chang et al., 2013) identified an ensemble of 1,578 δSct, both nearby field stars and cluster members in the Milky Way galaxy. The catalog is publicly available at https://vizier.u-strasbg.fr/viz-bin/VizieR-3?-source=J/AJ/145/132/table3.
The target list compiled by Chang et al., 2013 includes 718 targets from Rodriguez, Lopez-Gonzalez and Lopez de Coca, 2000 (46%) and 860 stars from other published literature (54%). The survey catalogs from which stars are extracted are: Hyppar-cos[1], the MAssive Compact Halo Object[2] (MACHO), the Optical Gravitational Lensing Experiment[3] (OGLE), the Robotic Optical Transient Search Experiment[4] (ROTSE), the All-Sky Automated Survey[5] (ASAS), the Taiwan-American Oc-cultation Survey (TAOS) and the General Catalog of the Variable Stars[6] (GCVS). Neither TESS (Ricker et al., 2014) nor K2 (Kepler follow-up, Howell et al., 2014) missions have been cited because in 2013 the two satellites were not operative yet, indeed, K2 mission started in 2014 and TESS was launched in 2018.

[1] http://tdc-www.harvard.edu/catalogs/hipparcos.html
[2] http://wwwmacho.anu.edu.au
[3] http://ogle.astrouw.edu.pl
[4] http://www.rotse.net
[5] http://www.astrouw.edu.pl/~gp/asas/
[6] http://www.sai.msu.su/gcvs/index.htm

The catalog is organized in columns and the most relevant for my purposes are:

- *Right ascension* (RA) and *Declination* (Dec) for each target referred to epoch J2000.0. Right ascensions are specified in hours, minutes and seconds (h:m:s) while declinations in days, minutes and seconds (d:m:s).
- *Apparent magnitudes* in the Johnson's B and V bands for all objects except for 17 δSct for which V magnitude is not provided (see Fig. 4.1a).
- *Periods* (see Fig. 4.1b) and *amplitudes* of pulsation corresponding to the dominant primary periodicity discarding the multiperiodic δSct stars[7]. When available amplitudes are computed as the full width of periodic variations in V band (ΔV), if not they are computed as the difference between the maximum and minimum V magnitude.
- *Spectral type* organized according to the catalog outlined by Skiff, 2009. The modern Morgan-Keenan classification is adopted. Chang and collaborators apply the S flag for spectroscopic spectral type and the P flag for photometric spectral type.
- *Binarity*[8] labeled as "1" if the δSct star is found in a binary stellar system, "0" if no companions are known. Of 1,578 catalogued δSct stars, 141 are found in binary systems.
- *Membership* describing the stellar population to which the target is belonging: Milky Way Field (MWF), Open Cluster (OC) or Globular Cluster member (GC), see Fig. 4.1a.

I plotted the figures cited and reported below using the Tool for OPerations on Catalogues And Tables (TOPCAT[9], Taylor, 2017). The two histograms have the purpose of summarizing some relevant properties of the catalog (Fig. 4.1a and 4.1b).

[7] Many δSct exhibit multiperiodicity due to simultaneous oscillations in both radial and non-radial modes.

[8] The majority of δSct stars in binary systems are found as eclising binaries.

[9] http://www.star.bris.ac.uk/~mbt/topcat/

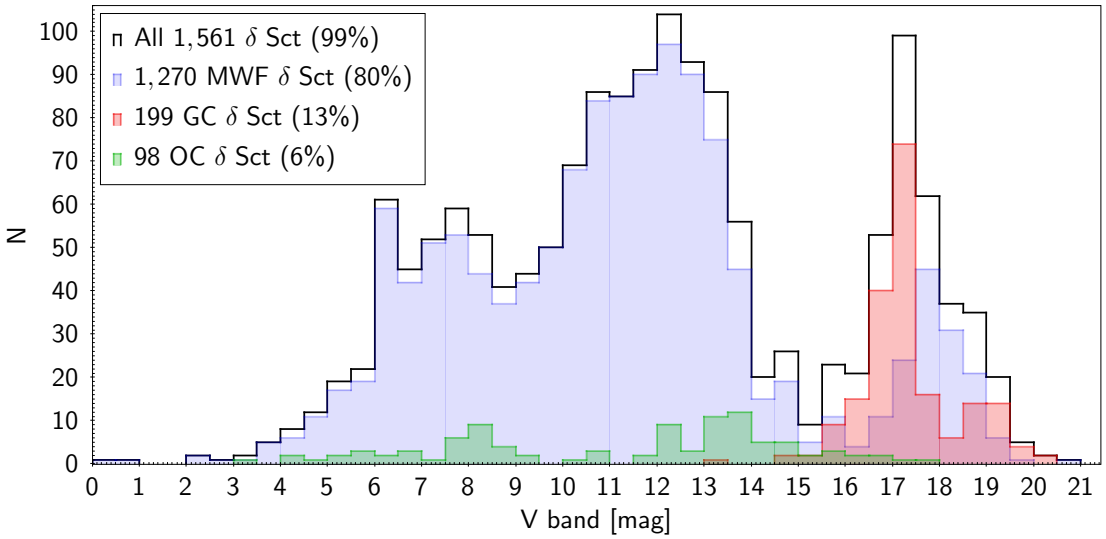

(a) Histogram of δSct from Chang et al., 2013 catalog as a function of their V magnitude. The black solid line marks the total amount of δSct for which the V magnitude is available. The blue, red and green shaded regions represent the count of subgroups MWF, GC and OC respectively.

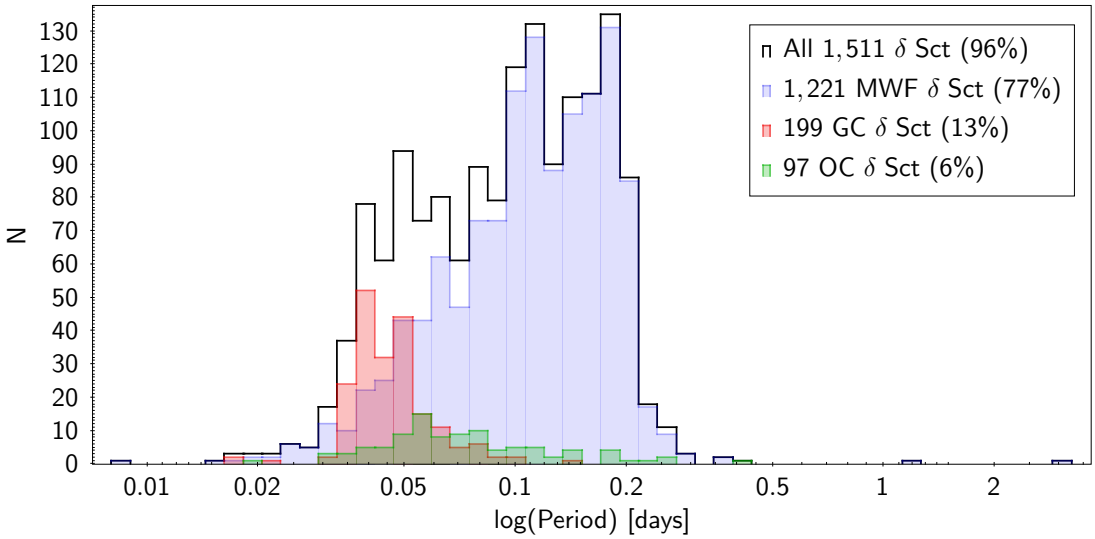

(b) Histogram of δSct from the Chang et al., 2013 catalog as a function of the period (in logarithmic scale). The black solid line marks the total amount of δSct for which the period is available. The blue, red and green shaded regions represent the count of subgroups MWF, GC and OC respectively. It is clear that most targets have a period in the range 0.02 - 0.25 days, typical of δSct stars.

4.2 Match with other catalogues

I skimmed the catalog by Chang and collaborators in order to select only the targets most suited for this work. Since I am interested in retrieving TESS light curves, I cross-matched the Chang catalog with the TESS CTL list (sectors 1-34) to identify only known δSct stars also observed by TESS at a high photometric cadence (2 min). For all the cross-matched stars, the following additional columns are then available:

- The target TIC name;
- TESS magnitude labeled as $T_{\rm mag}$;
- The number of TESS sectors where the star is observed ($N_{\rm sec}$).

I imposed further conditions on this subgroup of δSct:

- Exclusion of known binary stars (those with binarity column index = 1);
- $T_{\rm mag} < 11$ (bright stars for TESS);
- Long TESS observational baseline[10] translated in stars observed in more than one TESS sector, $N_{\rm sec} > 1$.

[10] As previously explained, a long observational baseline is required for an efficient application of the PT technique.

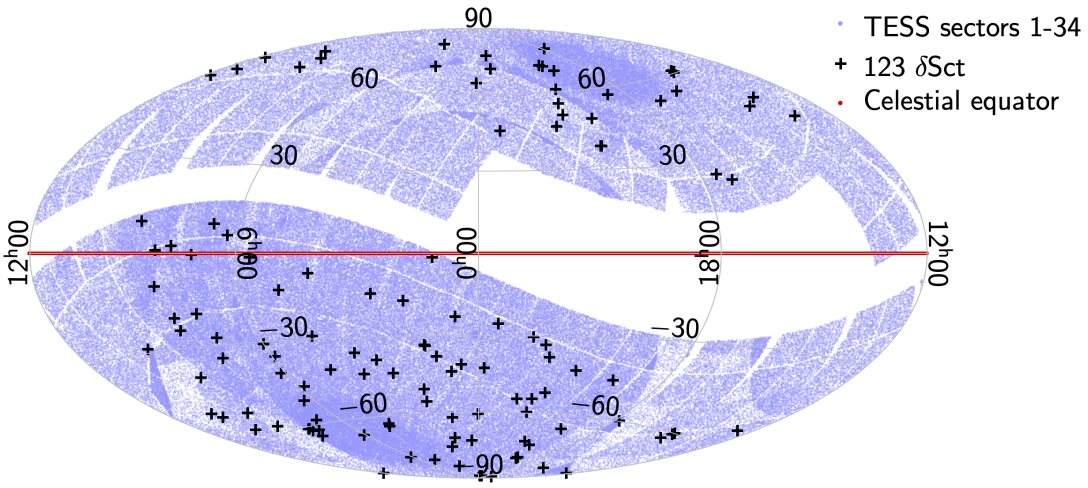

Figure 4.2: Preliminary δSct sample selection shown in Aitoff projection. The purple shaded area is the cumulative TESS coverage between sectors 1 to 34. The overplotted 123 black crosses are the selected bright, non-binary δSct stars having $T_{\rm mag} < 11$ and $N_{\rm sec} > 1$. The red solid line indicates the celestial equator.

Finally, I matched the resulting δSct list together with the table containing the TESS light curves to be downloaded.
In this context, I imposed an additional condition: only those δSct stars observed in seven or more TESS sectors are considered, given that a long observational baseline is strictly required for applying the PT technique (see section 2.3). As a result, I obtained a suitable list of 13 candidate stars whose TESS extracted light curves have been looked at in order to select only δSct with coherent and large-amplitude oscillation modes, e.g. HADS. Moreover, one of the 13 selected stars (TIC 141770299) is found to be catalogued as an eclipsing binary, therefore I immediately excluded it from the list because this work is interested only on single targets. Under these conditions, the list is reduced to just five δSct.

4.2.1 The final sample

Afterwards, I manually joined two additional targets to the provided list of δSct: Chang 134 (TIC 431589510) and Chang 349 (TIC 260654645). Both targets are included within the Chang catalog but they have a TESS magnitude slightly higher than the imposed magnitude threshold at $T_{\rm mag} < 11$, hence, initially, they were excluded from the selection. Even though this pair of δSct is quite faint in terms of

TESS magnitude, they both show pulsation amplitudes high enough to be classified as HADS (Antoci et al., 2019) and they are observed in many TESS sectors, resulting in a long observational baseline. These properties make them objects of interest for this work. In conclusion, it is worth it to include them in the final shortlist of seven suitable δSct stars summarized in Table 4.1.

Table 4.1: List of 7 suitable selected δSct stars

Star[a]	TIC[b]	Dec[c] [deg]	RA[c]	T_{eff}^{c} [K]	Parallax[c] [mas]	Spectral type[a]	δSct type[d]	T_{mag}^{b}	N_{sec}^{b}
V393 Car	364399376	−61.58	07h 59m 2.5s	7040.8	5.388	A7III	HADS	7.16	9
Chang 349	260654645	−57.81	06h 32m 45.2s	7232.0	0.610	–	HADS	12.44	17
Chang 134	431589510	−72.63	03h 22m 45.8s	7281.7	0.843	–	HADS	11.89	8
V435 Car	255548143	−51.24	06h 21m 50.0s	7766.0	14	A5V	envelope	6.55	7
HD 173844	359678383	+57.21	18h 44m 12.0s	7303.1	5.654	A2	envelope	8.4	13
GW Dra	329153513	+77.38	17h 53m 4.0s	6769.5	2.709	F2	envelope	8.9	12
UZ Ret	38515566	−63.16	04h 11m 3.8s	6652.5	2.927	F0	envelope	8.85	8

Notes – [a]: Properties available on SIMBAD (http://simbad.u-strasbg.fr/simbad/).
[b]: Properties extrapolated from the crossmatch between the catalogue of Chang & collaborators (2013) and the TESS CTL.
[c]: Dec, RA and effective temperature provided by Gaia Data Release 2 (DR2) archive available at https://gea.esac.esa.int/archive/.
[d]: The first three δSct stars are classified as "HADS" by Antoci et al., 2019 whereas the "envelope" property is derived from TESS light curves.

Chapter 5
Astrophysical parameters

Having selected a suitable list of δSct stars (see Table 4.1), it is necessary for the subsequent modeling to add some missing astrophysical parameters about those targets such as effective temperature, luminosity and mass.

5.1 Empirical relations for the estimation of stellar masses

δSct variables typically have masses in the range 1.2 - 2 $M_\odot$ (S. Murphy, 2015). After the outline of a list of 7 suitable δSct, I estimated their masses according to the relation derived by Moya et al., 2018. Moya and collaborators took into account an amount of 934 stars (most of them being at the main-sequence evolutionary stage) whose parameters are well defined thanks to asteroseismology, interferometry and studies about eclipsing binaries.
Asteroseismology gives accurate characterization of stellar inner structures via the study of stellar pulsations. Of great relevance for the review of Moya and collaborators, were the CoRoT (Moutou et al., 2013) and Kepler missions which delivered ultra-high-accuracy photometry and therefore very accurate measurements of frequencies of pulsations, especially for Solar-type stars.
Interferometry is based on the concept that to resolve accurately the angular diameter of stars the solution lies in combining signals from an array of optical telescopes (better spatial resolution) resulting in a unique signal coming from one telescope having an aperture diameter equal to the full extension of the array.
Finally, eclipsing binary systems can be characterized by means of spectroscopic and photometric data: from the first the mass ratio is derived thanks to radial velocity measurements, from the latter the radius ratio is inferred from photometric light curves; from the combination of the two techniques, radii and masses can be derived in physical units, along with the eccentricity and the orbital inclination of the system. Moreover, if the effective temperatures are known, the luminosities of both stars can be measured. Therefore, having good estimates of those stellar parameters, they derived empirical relations to evaluate stellar masses as a func-

tion of other quantities. In particular, in this work I used the following equation to estimate the masses of the provided δSct:

$$\log_{10}(M) = -a + b\,T_{\rm eff} + c\log_{10}(L), \tag{5.1}$$

where M, $T_{\rm eff}$ and L are the stellar mass, effective temperature and luminosity, respectively. This relation is valid within the range of temperatures 4780 K $\leq T_{\rm eff} \leq$ 10990 K. The coefficients a, b and c are tabulated by Moya et al., 2018 together with their errors. Values have been chosen according to the relation function assumed for this work, that is $\log_{10}(M) = f(T_{\rm eff} + \log_{10}(L))$.

Table 5.1: Coefficients and respective errors computed by Moya et al., 2018 using the GLSME (Generalized Least Squares with Measurement Error) algorithm.

Coefficient	Value	σ
a	-0.119	0.003
b	2.14×10^{-5}	5×10^{-7}
c	0.1837	0.0011

In conclusion, stellar masses (in Solar mass unit) are computed as:

$$M = 10\text{^}(-0.119 + 2.14 \times 10^{-5} T_{\rm eff} + 0.1837\ \ \log_{10}(L)). \tag{5.2}$$

I propagated the uncertainties on the masses as the quadratic sum of the partial derivatives considering errors on coefficients, temperatures and luminosities. Moreover, I added in quadrature a relative error of 8.55%, according to the total relative accuracy estimated by the authors for the function used.

5.1.1 Chang 349, UZRet, V393 Car, V435 Car, HD 173844, GW Dra

The aforementioned equation (Eq. 5.1) obtained by Moya et al., 2018 depends on both the effective temperature and luminosity of each target. I used it in order to compute the mass of Chang 349, UZRet, V393 Car, V435 Car, HD 173844 and GW Dra, for which accurate spectroscopic measurements are lacking. $T_{\rm eff}$ and L with uncertainties are tabulated in the Gaia Data Release 2 (Gaia DR2)[1] archive.

[1]Gaia is an ESA sky-survey mission operative since 2013 providing high quality photometry (passband $\sim$ 330-1050 nm) and high resolution spectroscopy ($\sim$ 845-872 nm). Gaia DR2 was published in 2018 after 22 months of observation.

Table 5.2: Effective temperature and luminosity with errors archived in Gaia DR2 for each target selected.

Star	$T_{\rm eff}$ [K]	$\sigma_{T_{\rm eff}}$ [K]	L [$L_\odot$]	σ_L [$L_\odot$]
V393 Car	7040	280	27.44	0.32
Chang 349	7232	367	14.61	0.96
V435 Car	7766	292	8.09	0.02
HD 173844	7303	149	8.29	0.07
GW Dra	6770	131	21.34	0.38
UZRet	6653	248	18.98	0.29

I computed the uncertainties on $T_{\rm eff}$ and L as the semidifference between the upper ($84^{\rm th}$) and lower ($16^{\rm th}$) percentiles reported in Gaia DR2 archive: $\sigma = (84^{\rm th} - 16^{\rm th})/2$.

5.1.2 Chang 134

In the case of Chang 134 the relation derived by Moya et al., 2018 cannot be used to determine the target mass, since only the effective temperature is available on Gaia DR2 archive. Therefore, the mass I assumed for Chang 134 is the one computed by Queiroz, Anders, Chiappini et al., 2020. The authors catalogued extinction, distances and the main spectroscopic parameters of a list of 388,815 stars derived combining APOGEE-2 survey DR16[2] high-spectroscopic measurements with broad-band photometric data taken by different sources. Finally, stellar parameters are derived as the posterior distribution returned by the Bayesian isochrone-fitting code `StarHorse` (Queiroz, Anders, Santiago et al., 2018). Hence, the accepted mass for Chang 134 is reported on VizieR[3] as the $50^{\rm th}$ percentile of the `StarHorse` stellar mass probability distribution function and I estimated the uncertainty as the semidifference between upper and lower percentiles, the $84^{\rm th}$ and the $16^{\rm th}$ of the mass probability distribution, respectively.

[2] https://www.sdss.org/surveys/apogee-2/
[3] https://vizier.u-strasbg.fr/viz-bin/VizieR

In conclusion, the derived stellar masses with corresponding uncertainties are reported in the following Table 5.3.

Table 5.3: Masses of the 7 selected δSct

Star	$M \pm \sigma_M$ [$M_\odot$]
V393 Car	1.98 ± 0.17
Chang 349	1.78 ± 0.16
Chang 134	1.38 ± 0.03
V435 Car	1.64 ± 0.14
HD 173844	1.60 ± 0.14
GW Dra	1.86 ± 0.16
UZRet	1.81 ± 0.16

How it is expected for δSct in the bottom of the instability strip, all values are within the range of mass typical of δSct variables which is 1.2 - 2 $M_\odot$ (S. Murphy, 2015).
Except for Chang 134, luminosities, temperatures and respective uncertainties have been derived for all targets. Therefore for these δSct, I plotted the mass-luminosity relation with proper computed error bars on varying of the effective temperature (Fig. 5.1).

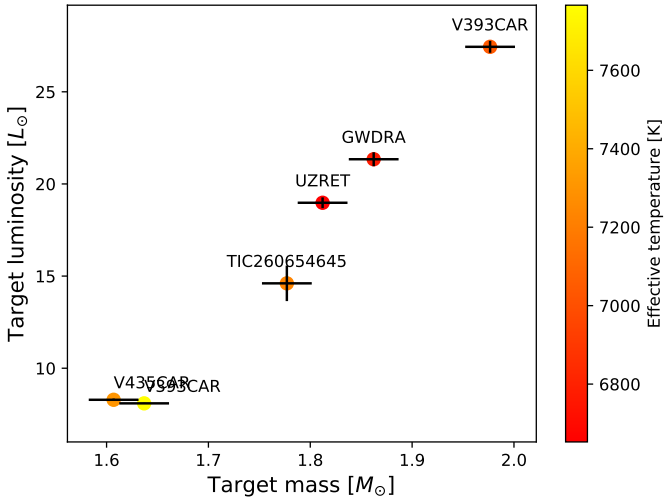

Figure 5.1: Mass-luminosity relation for 6 targets on varying of T_{eff}. Chang 134 is missing because its luminosity is not reported by Gaia DR2.

Since Chang 134, Chang 349, UZRet, V393 Car, V435 Car, HD 173844 and GW Dra were all observed by Gaia DR2 mission at the reference epoch J2015.5, I plotted a superposition of Gaia DR2 J2015.5 catalog and of my targets of interest in a color-magnitude diagram (CMD, see Fig. 5.2) without correcting for differential reddening which typically affects every CMD. The green squares are the 7 δSct located in the low region of the instability strip, nearby the ZAMS. Their computed masses are consistent with the expected values for main sequence δSct (1.2 - 2 $M_{\odot}$), see properties in section 2.2.

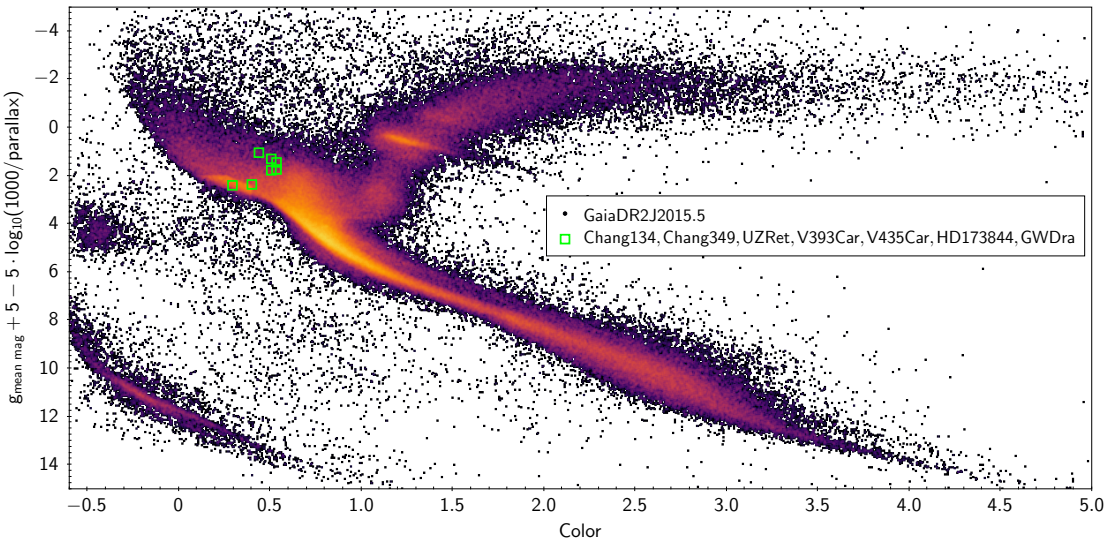

Figure 5.2: CMD of Gaia DR2 J2015.5 survey considering Gaia photometric passband (G $\sim$ 330-1050 nm) and color crossmatched with TESS CTL (sectors 1-34). No differential reddening correction is applied to the diagram. Highlighted in green the 7 δSct of interest for this work. The targets are clearly located in the low instability strip, nearby the ZAMS.

Chapter 6
Harmonic analysis

In this chapter I describe the harmonic analysis carried out for the three selected Milky Way field HADS (Chang 134, V393 Car, Chang 349) from our sample. Those were chosen as the initial targets of our pilot study because they are the most favorable pulsators to be studied, since they exhibit short-period oscillations (typically 1-3 hours) and high pulsation amplitudes i.e. peak-to-peak flux variation exceeding 0.3 magnitudes (see Chapter 2). In this case, the PT technique yields a very high signal-to-noise ratio, theoretically able to detect phase shifts of the order of fraction of seconds. However, I keep the other four selected δSct of our sample as objects of interest for future applications of the PT technique, looking for a more generalized study involving other types of pulsators (see subsection 7.3.1).
The entire harmonic analysis was carried out exploiting the `VARTOOLS` Light Curve Analysis Program[1] by Hartman and Bakos, 2016. `VARTOOLS` 1.39 (released October 30, 2020) is a command line tool for filtering, modelling and manipulating astronomical time-series data.

6.1 Common algorithm

6.1.1 Light curve pre-conditioning and filtering

As a first step to pre-condition the light curves for the subsequent analysis, I filtered and sorted the original TESS light curves extracted from each observing sector and sampled every ∼2 minutes according to the short-cadence strategy. I chose to extract the measured PDCSAP flux since it results in cleaner light curves by removing long term trends (see subsection 3.1.4); afterwards, I converted the flux and its error to magnitudes, using the standard Pogson formula. Moreover, I cut the light curves according to an iterative clipping factor of 15 σ, chosen arbitrarily, to discard unreasonable points. By default the sigma-clipping is performed with respect to the mean. At last, I removed from the light curve all defective points having quality factor $q \neq 0$.
Every ∼13.7 days (approximately two weeks) the TESS spacecraft is at the perigee

[1] https://www.astro.princeton.edu/~jhartman/vartools.html

($\sim$17 $R_\oplus$) of its elliptical orbit around the Earth (see Fig. 6.1). At this location the satellite stops its science mission and orients to point the Ka-band high-gain antenna towards one of the three NASA Deep Space Network (DSN) stations for data downlink lasting about 3 hours. After data download is completed, TESS re-orients back to the science mission resuming the sky-survey for other two weeks. The entire operation takes about 1 day which is consistent with the observed gap in the time-series (Fig. 6.2).

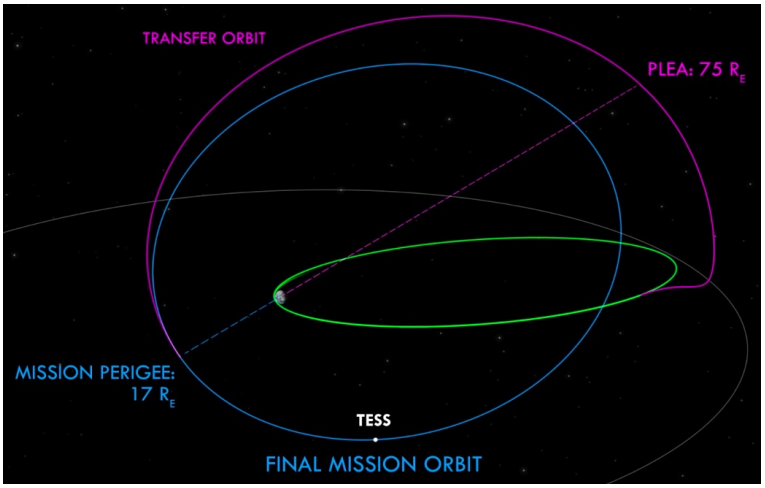

Figure 6.1: Schematic view of the mission orbit insertion. At first TESS was put in an initial parking orbit around the Earth at an altitude of about 600 Km. As a second step, the solid rocket motor pushed the satellite in an higher first phasing orbit having the nominal apogee at 250,000 Km (green orbit). At the perigee of the first phasing orbit TESS speed up to increase the apogee until a final apogee of 400,000 Km. At that point, TESS exploited the lunar gravity to perform a lunar fly-by for an orbital transferring into the so called PLE (Post-Lunar-Encouter) transfer orbit (purple line). At PLEP (Post-Lunar-Encouter-Perigee, $\sim$ 17 $R_\oplus$) TESS spacecraft performed the period adjustment to reduce the mission orbital period to be $\sim$ 13.7 days at 2:1 resonance with the Moon's orbit (final mission orbit, blue ellipse).
Image credit: https://tess.mit.edu/science/

I took advantage of this existing gap to split each sector into two so called "orbits" of $\sim$14 days. The two orbits together cover about 27 days of observation which is the standard period of observation per every TESS sector. I report below an example of one light curve of Chang 134 extracted from the first TESS sector in 2018 to show the gap due to downlinks (Fig. 6.2) and the total light curve of Chang 134 considering every TESS sector where the star is observed (Fig. 6.3).

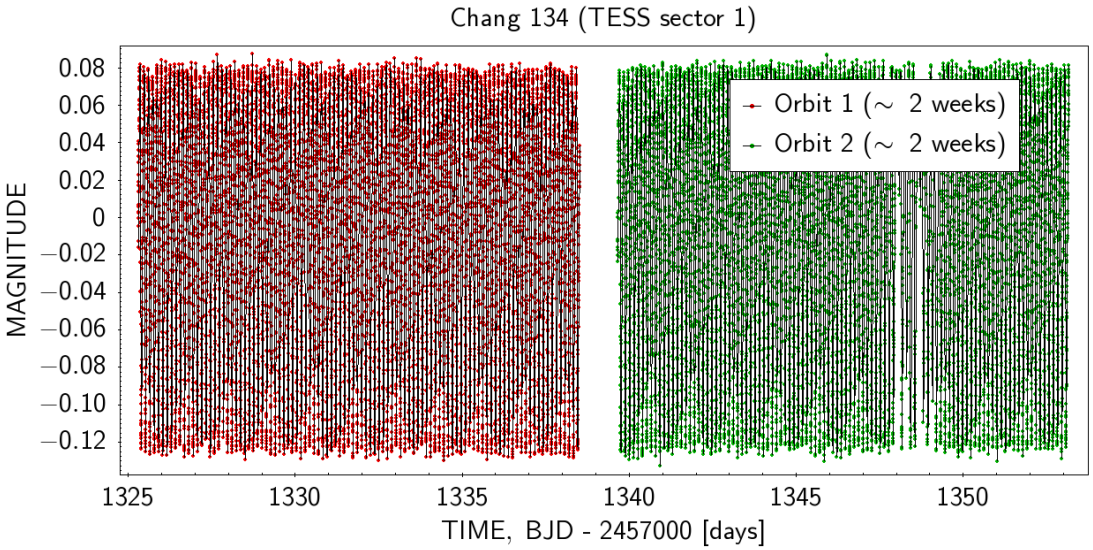

Figure 6.2: Light curve of Chang 134 from sector 1. In red and green the first and second 2-weeks orbit, respectively. In the middle of the time-series is clearly visible the ∼1-day gap as a consequence of the remote operation of data download.

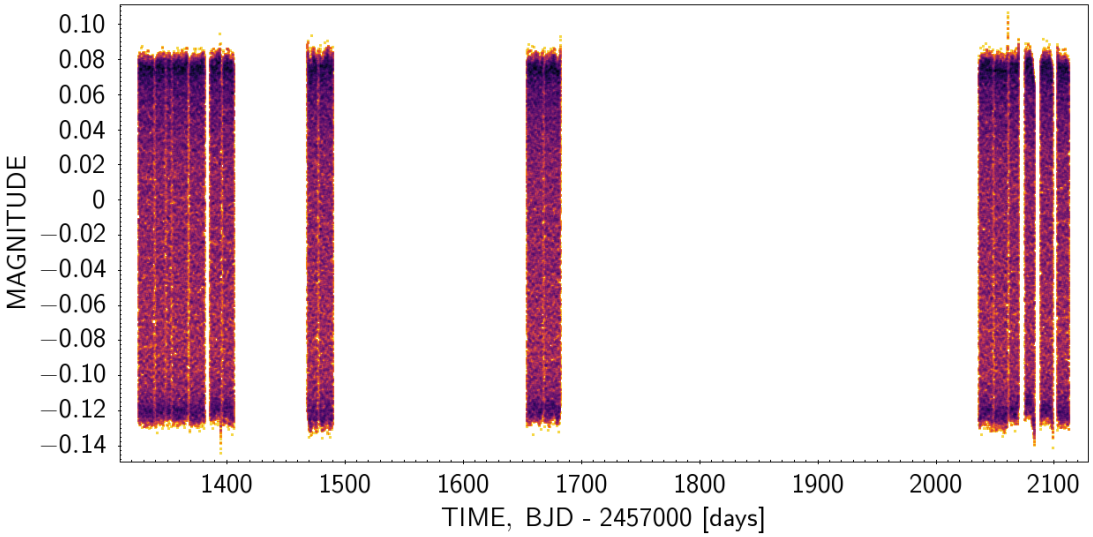

Figure 6.3: Total light curve of Chang 134 considering every TESS observing sector.

6.1.2 The Lomb-Scargle Periodogram

The Lomb-Scargle (LS) periodogram (VanderPlas, 2018) is a widespread tool for searching and characterizing periodicity in time series. In particular, in this thesis

work, I made use of the Generalized Lomb-Scargle (GLS, Zechmeister and Kürster, 2018) periodogram, since it is the LS version implemented in `VARTOOLS` program. Compared to LS, GLS provides much more accurate frequencies, is less sensitive to aliasing and returns a better spectral intensity determination.
To fully understand the LS periodogram approach it is necessary to introduce the Fourier analysis. Given a continuous time-signal *g(t)*, its Fourier transform is defined as:

$$\mathcal{F}(g) \equiv \hat{g}(f) = \int_{-\infty}^{+\infty} g(t) e^{-2\pi i f t} dt, \tag{6.1}$$

where $i \equiv \sqrt{-1}$ is the imaginary unit. Some relevant properties are:

- The Fourier transform is a linear operation.
  Given a constant A and functions *f(t)*, *g(t)*, is true that:

$$\mathcal{F}\{f(t) + g(t)\} = \mathcal{F}\{f(t)\} + \mathcal{F}\{g(t)\}, \tag{6.2}$$

$$\mathcal{F}\{Af(t)\} = A\mathcal{F}\{f(t)\}. \tag{6.3}$$

- The Fourier transform of a sinusoid with frequency f_0 is a sum of delta functions at $\pm f_0$.

$$\mathcal{F}\{e^{2\pi f_0 t}\} = \delta(f - f_0), \tag{6.4}$$

  where $\delta(f) \equiv \int_{-\infty}^{+\infty} e^{-2\pi i f x} df$ is the Dirac delta function.

- A time shift imparts a phase in the Fourier transform.

$$\mathcal{F}\{g(t - t_0)\} = \mathcal{F}\{g(t)\} e^{2\pi i f t_0}. \tag{6.5}$$

These properties make Fourier transform an optimal approach to study periodicity in a measured signal.
What is useful by constructing a periodogram is to compute the power of the Fourier transform of a given time signal $g(t)$. The power spectral density (PSD) or power spectrum quantifies the contribution of each single frequency to the global signal and it is defined as:

$$\mathcal{P}_g \equiv |\mathcal{F}\{g(t)\}|^2. \tag{6.6}$$

Once I derived the GLS power spectrum as a function of the frequency of pulsation, I extracted the dominant pulsation period (or frequency) which corresponds to the peak showing the highest power within the periodogram. Since the LS periodogram is used to identify the frequency pattern of a pulsator (i.e. how many frequency series, pulsation modes and harmonics belong to the pulsator), the most prominent peak coincides with the fundamental frequency of the dominant stellar pulsation

mode and the consecutive equally spaced peaks are the respective harmonics of the fundamental frequency belonging to the same pulsation mode.

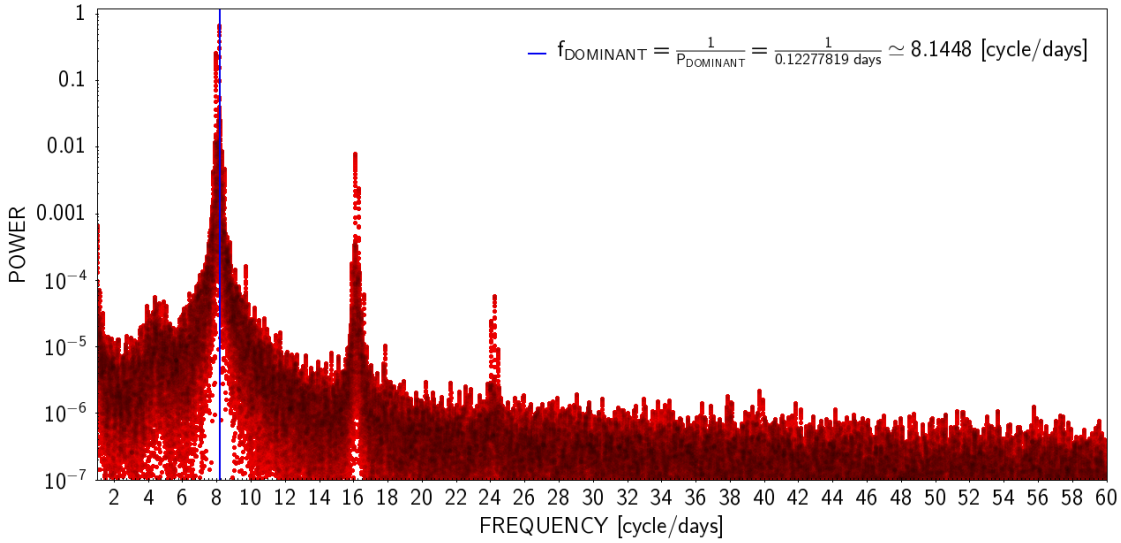

Figure 6.4: GLS Periodogram of δSct UZRet (TIC 38515566). The vertical blue line highlights the most prominent peak corresponding to the dominant series of frequencies of one pulsation mode.

6.1.3 Harmonic fit: least-square approach

At first, I fitted a series of harmonic functions to the TESS light curve, by fixing their frequency at the dominant peak found by the GLS periodogram and its harmonics. In this context, the periodogram is whitened at each peak namely it is recomputed before searching the next period peak. This initial fit was carried out through a traditional least-squares approach performed according to the `VARTOOLS` command `-Killharm` that whitens the light curve over one or more periods by fitting and subtracting a function of the form:

$$\mathrm{K(t)} = \sum_{i=1}^{N_{\mathrm{PER}}} \left\{ \sum_{k=0}^{N_{\mathrm{HARM,i}}} \left[a_{ik} \cdot \sin(2\pi(k+1) \cdot f_i \cdot t) + b_{ik} \cdot \cos(2\pi(k+1) \cdot f_i \cdot t) \right] + \right.$$
$$\left. + \sum_{k=0}^{N_{\mathrm{SUBHARM,i}}} \left[c_{ik} \cdot \sin\left(\frac{2\pi \cdot f_i \cdot t}{k+1} \right) + d_{ik} \cdot \cos\left(\frac{2\pi \cdot f_i \cdot t}{k+1} \right) \right] \right\}, \tag{6.7}$$

where N_{PER} is the number of periods of pulsation, N_{HARM} are the higher-harmonics corresponding to integer multiples of each dominant period/frequency (frequencies

of $2*f_i, 3*f_i, ..., (N_{\rm HARM}+1)*f_i$) and $N_{\rm SUBHARM}$ are the respective sub-harmonics (frequencies of $f_i/2, f_i/3, ..., f_i/(N_{\rm SUBHARM}+1)$). I took into account only the first 10 harmonics of the fundamental frequency, neglecting the sub-harmonics whose flag is set to zero. a_{ik}, b_{ik}, c_{ik} and d_{ik} are the coefficients of the trigonometric functions whose values, together with the period and the mean magnitude of the light curve, are returned as default outputs of the fit. In addition, I setup `VARTOOLS` to return also amplitudes and phases of the pulsation, e.g. in the form $A_k = \sqrt{a_k^2 + b_k^2}$ and $\phi_k = \arctan2(-b_k, a_k)/2\pi)$[2], respectively.

From the best-fit pulsation parameters computed for each one-orbit (two-weeks) segment of the TESS light curve by the linear model, I constructed the $(O-C)$ phase-shift diagram to search for timing drifts induced by LTEs. The $(O-C)$ diagram reports residuals in seconds by converting phase shifts in times as:

$$O - C = \frac{(\phi_0 - \phi_{0,\ \rm mean}) \cdot P_{\rm dominant} \cdot 86,400}{N}, \tag{6.8}$$

where ϕ_0 is the fundamental phase returned by the least-squares fit, $\phi_{0,\ \rm mean}$ is the mean fundamental phase computed over all TESS light curves, $P_{\rm dominant}$ is the dominant pulsation period obtained from the GLS periodogram, N is an integer number assumed to be equal to unity for the fundamental phase ($N = 2$ for the first harmonic, $N = 3$ for the second harmonic, etc.) and 86,400 is the conversion factor from days to seconds.

6.1.4 Harmonic fit: refined MCMC model

As a first step, to perform a more accurate harmonic analysis, I "cleaned" the TESS light curves by discarding parts affected by systematic errors. At the far ends of almost each orbit, there are departures with respect to the expected trend of the series given by the settling of the satellite during the remote operation of data download. To get rid of such drifts, I manually selected the time intervals affected by such problems and I removed them from the light curve. I report below (Fig. 6.5) a representative example of the cleaning (the final selection is plotted with black points) performed on a segment of the light curve of Chang 134 where drifts are pretty evident (red dots).

[2]Taken two non-null arguments x and y, the function $\arctan2(x, y)$ or $\mathrm{atan2}(x, y)$ defines the angle in the Euclidean plane between the x-axis and the vector from the origin to the point of coordinates $(x, y) \neq (0, 0)$.

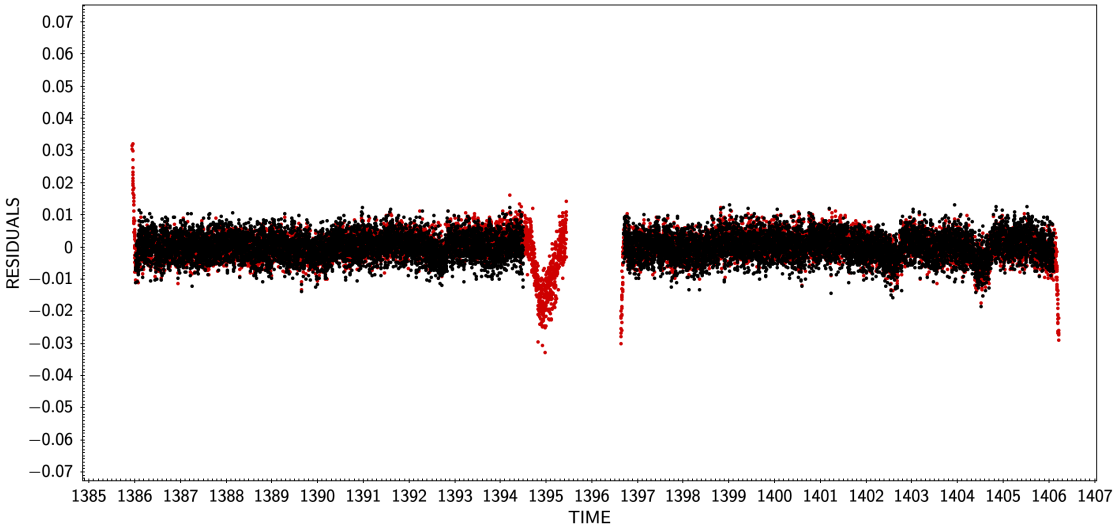

Figure 6.5: Zoom-in of the light curve of Chang 134. In red the original light curve whose departures at the beginning and at the end of the orbits are evident. In black the cleaned light curve where drifts are manually removed.

In order to get a more accurate model with respect to our preliminary least-square fit, I implemented a model function where the usual combination of harmonic functions (with amplitude and phase as free parameters for each frequency probed) is summed to a quadratic baseline, i.e. a parabola with three more free parameters. I added a quadratic baseline to take into account systematic uncertainties on longer timescales, i.e. days-weeks, due to drifts of the satellite while pointing a target and/or to thermal effects. This enhanced model is fitted with a more sophisticated algorithm: a differential evolution Monte Carlo Markov Chain (MCMC, Speagle, 2019) code to sample the posterior distribution of the best-fit pulsation parameters to obtain uncertainties of the phase shifts.
The non-linear model I adopted, as a function of time t as the only independent variable, is therefore a combination of one parabola and N sine waves. In the specific case where I fit the fundamental mode and its first two harmonics, the model can be explicitly written as:

$$\begin{aligned}\mathrm{NL(t)} = b_0 + b_1 \cdot (t - t_{\mathrm{median}}) + b_2 \cdot (t - t_{\mathrm{median}})^2 + A_0 \cdot \cos\left(\frac{2\pi t}{P_{\mathrm{dominant}}} + 2\pi\phi_0\right) + \\ + A_1 \cdot \cos\left(\frac{2\pi t}{2 \cdot P_{\mathrm{dominant}}} + 2\pi\phi_1\right) A_2 \cdot \cos\left(\frac{2\pi t}{3 \cdot P_{\mathrm{dominant}}} + 2\pi\phi_2\right),\end{aligned} \tag{6.9}$$

where b_0, b_1 and b_2 are the coefficients of the parabola; A_0, A_1 and A_2 are the amp-

litude of the fundamental frequency and of its harmonics, respectively; ϕ_0, ϕ_1 and ϕ_2 are the phase of the fundamental frequency and of its harmonics, respectively; P_{dominant} is the dominant period of pulsation extracted from the GLS periodogram as described previously in section 6.1.2.

According to the Bayesian approach, the parameters I am fitting are not usually completely unknown before the fit, but rather they are distributed across a distribution of values according to the so called "prior probability distribution". Priors I assumed for phases and amplitudes are uniform and centered on initial guesses which are the computed mean of values returned by the previous least-squares fit I performed according to the `-Killharm` routine. The assigned initial guesses are the starting point for the chains to perform the fit. MCMC generates random samples according to the priors I gave initially, then creates a chain of correlated parameter values over N iterations to compute the posterior probability distribution function defined by the Bayes' theorem:

$$P(x|D) = \frac{P(D|x)P(x)}{P(D)}, \tag{6.10}$$

where $P(x|D)$ is the posterior conditional probability of the model parameters given the data, $P(D|x)$ is the likelihood i.e. the conditional probability of observing the data given the model parameters, $P(x)$ is the prior probability and $P(D)$ is the data probability.

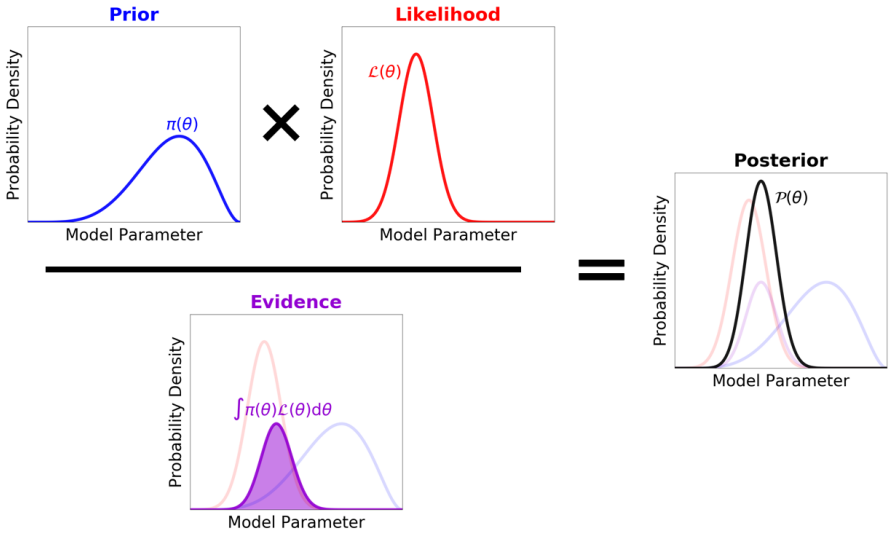

Figure 6.6: Illustration of the Bayes' theorem extracted from Speagle, 2019.

From the resulting values and their associated uncertainties, computed individually

for each one-orbit (two-week) segment of the TESS light curve, I constructed, for the fundamental phase, the $(O-C)$ phase-shift diagram to search for timing drifts induced by LTEs. The $(O-C)$ diagram reports residuals in seconds by converting phase shifts in times as:

$$O - C = \frac{(\phi_0 - \phi_{0,\,\mathrm{mean}}) \cdot P_{\mathrm{dominant}} \cdot 86\,400}{N}, \tag{6.11}$$

where ϕ_0 is the fundamental phase returned by the MCMC fit, $\phi_{0,\,\mathrm{mean}}$ is the mean fundamental phase computed over all TESS light curves, P_{dominant} is the dominant pulsation period obtained from the GLS periodogram, N is an integer number assumed to be equal to unity for the fundamental phase ($N = 2$ for the first harmonic, $N = 3$ for the second harmonic, etc.) and 86,400 is the conversion factor from days to seconds.

In conclusion, the improved model (which includes a quadratic baseline) combined with an MCMC analysis is favoured because it returns properly-estimated error bars and correlations between the resulting best-fit pulsation parameters. Moreover, it is consistent with the least-squares model, therefore a more accurate approach is preferred in my science case (see results in section 6.2).

6.2 Algorithm applied to the three HADS

I applied the previously illustrated algorithm to each of the three HADS stars selected in Chapter 4: Chang 134, V393 Car and Chang 349.
I show the results in increasing order of complexity of the observed pulsation pattern.

6.2.1 Chang 134

Chang 134 (TIC 431589510) is an HADS having an estimated mass of 1.38 ± 0.03 $M_{\odot}$[3]. Its TESS magnitude is 11.89 (therefore lying on the faint side of our sample) and it was observed in 8 non-consecutive TESS sectors (1, 2, 3, 6, 13, 27, 28, and 29) from 2018 until 26 August-22 September 2020 (Year 1, 2 and partially Year 3 of the mission). Chang 134 was re-observed again in sector 33 (17 December 2020 to 13 January 2021) and in sector 36 (7 March 2021 to 2 April 2021) but I did not included the latter two sector in my analysis since those light curves were not available for download when I started the harmonic analysis. Looking at the forthcoming sectors (up to sector 55, 5 August 2022 to 1 September 2022), Chang

[3]See Chapter 5.

134 could be re-observed[4].
From the spectral frequency pattern, Chang 134 is the simplest possible δSct pulsator since it exhibits one radial mode resulting in a single dominant frequency series (fundamental and the corresponding equally-spaced harmonics) as can be seen in the extracted GLS periodogram (Fig. 6.7).

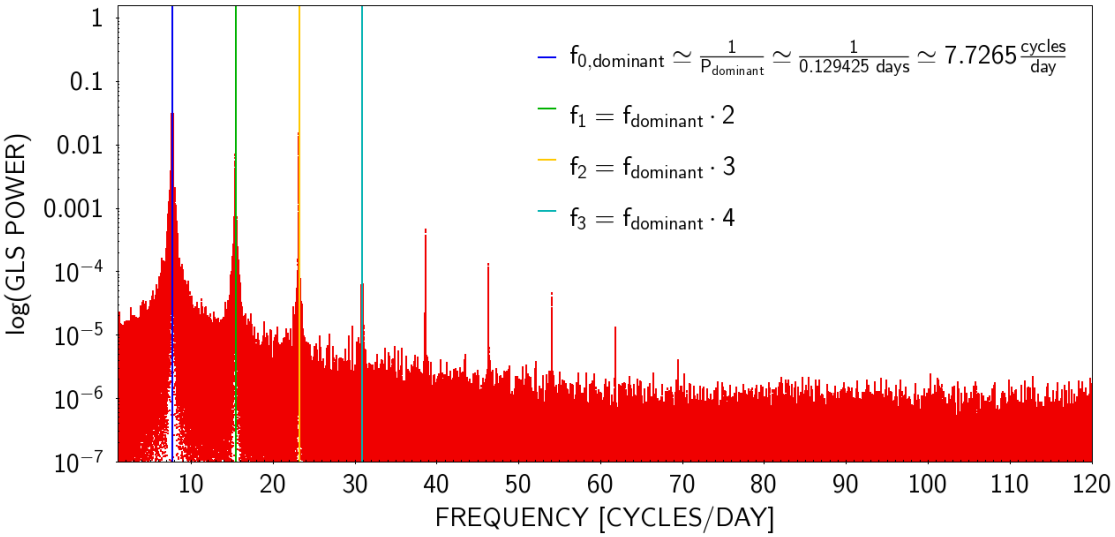

Figure 6.7: GLS Periodogram of Chang 134. The blue vertical line highlights the strongest frequency peaks within the diagram and the following coloured vertical lines indicates first three equally-spaced harmonics.

The strongest peak in the GLS periodogram corresponds to a dominant pulsation period of $\simeq 0.129$ days $\simeq 3.1$ hours or equivalently to a frequency of $\simeq 7.7265$ cycles/day. A pulsation period resulting in a few hours is fully consistent with oscillating properties of HADS stars. The harmonics of the dominant series (colored vertical lines in the periodogram) are integer multiples of the estimated fundamental pulsation frequency.
As described in details in section 6.1, after computing the GLS periodogram, I fixed the estimated fundamental frequency to perform a least-squares regression of the photometric TESS light curve (see subsection 6.1.3). Furthermore, I carried out an MCMC analysis as described in subsection 6.1.4 to refine the fitting with respect to the traditional least-squares method. The resulting $(O-C)$ diagrams showing the phase shifts obtained by both models are combined in the following graph (Fig. 6.8).

[4]Informations about the scheduled observations available at https://heasarc.gsfc.nasa.gov/cgi-bin/tess/webtess/wtv.py?Entry=TIC+431589510

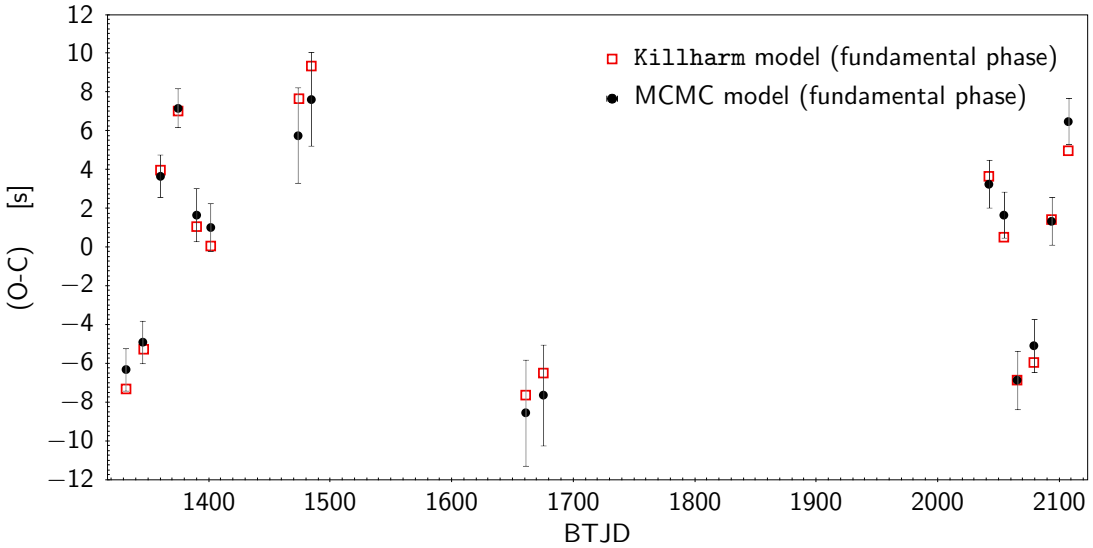

Figure 6.8: Resulting $(O-C)$ diagram of Chang 134. Red squares are returned by simple least-square regression as described in subsection 6.1.3, black dots with errorbars are the result of the MCMC fits as described in subsection 6.1.4.

The $(O-C)$ diagram illustrates phase shifts (in seconds) as the difference between observed fundamental phases, derived from the harmonic analysis I carried out on TESS light curves of Chang 134, and the expected phases, corresponding to the mean computed values, as a function of time in BTJD. In the figure above (Fig. 6.8) are shown 16 data points corresponding to two points for each TESS light curve, i.e. two points every observing sector (8 in case of Chang 134), one point for orbital segment (∼two weeks). The distribution of phase shifts within the residuals diagram suggests a sinusoidal periodic trend namely LTEs induced by a secondary body perturbing Chang 134. I will discuss the origin of the LTEs and the nature of the perturber in Chapter 7.

6.2.2 V393 Car

V393 Car (TIC 364399376) is an HADS having an estimated mass of 1.98 ± 0.17 $M_{\odot}$[5]. Its TESS magnitude is 7.16 and it was observed in 9 non-consecutive TESS sectors (1, 4, 7, 8, 10, 11, 27, 28 and 31) from 2018 until 2020 (Year 1, 2 and partially Year 3 of the mission). V393 Car was re-observed in sector 34 (13 January 2021 to 9 February 2021), 35 (9 February 2021 to 7 March 2021), 36 (7 March 2021 to 2 April 2021), 37 (2 April 2021 to 28 April 2021) and in sector 38 (28 April 2021 to 26 May 2021). I did not included the latter five sectors in my

[5]See Chapter 5.

analysis since those light curves were not available for download when I started the harmonic analysis. Looking at the forthcoming sectors (up to sector 55, 5 August 2022 to 1 September 2022), V393 Car could be re-observed[6].
The frequency pattern shows one dominant radial pulsation mode and also some other much weaker peaks corresponding to separate or mixed modes.

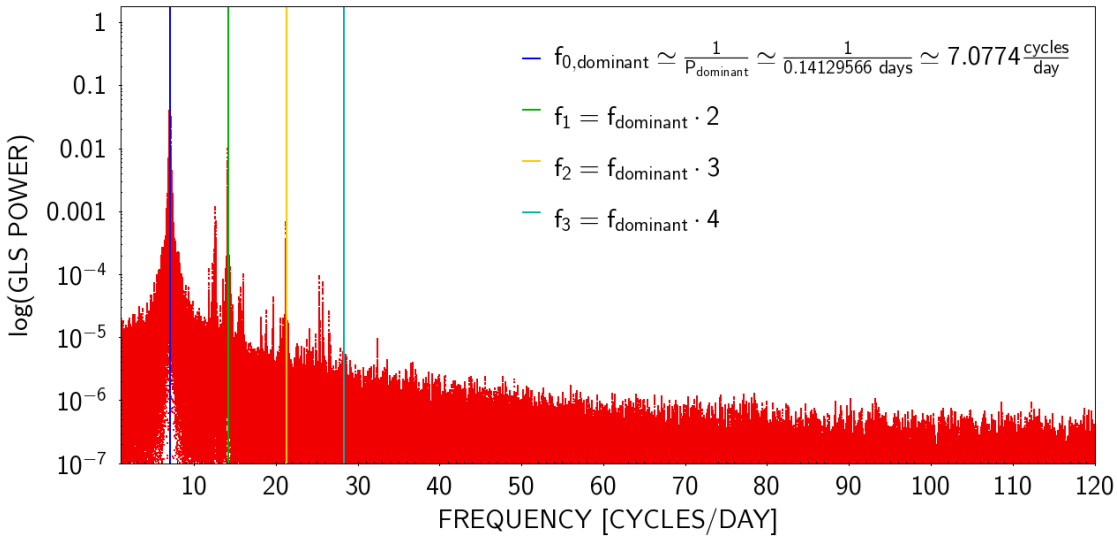

Figure 6.9: GLS Periodogram of V393 Car. The blue vertical line highlights the strongest frequency peaks within the diagram and the following coloured vertical lines indicates first three equally-spaced harmonics.

The strongest peak in the GLS periodogram corresponds to a dominant pulsation period of $\simeq 0.14$ days $\simeq 3.4$ hours or equivalently to a frequency of $\simeq 7$ cycles/day. A pulsation period resulting in a few hours is fully consistent with oscillating properties of HADS stars. The harmonics of the dominant series (colored vertical lines in the periodogram) are integer multiples of the estimated fundamental pulsation frequency.
According to the harmonic analysis described in details in section 6.1, the resulting $(O-C)$ diagrams showing the phase shifts obtained by both the traditional least-squares regression (see subsection 6.1.3) and the MCMC analysis, as described in subsection 6.1.4, are combined in the following graph (Fig. 6.10).

[6]Informations about the scheduled observations available at https://heasarc.gsfc.nasa.gov/cgi-bin/tess/webtess/wtv.py?Entry=TIC+364399376

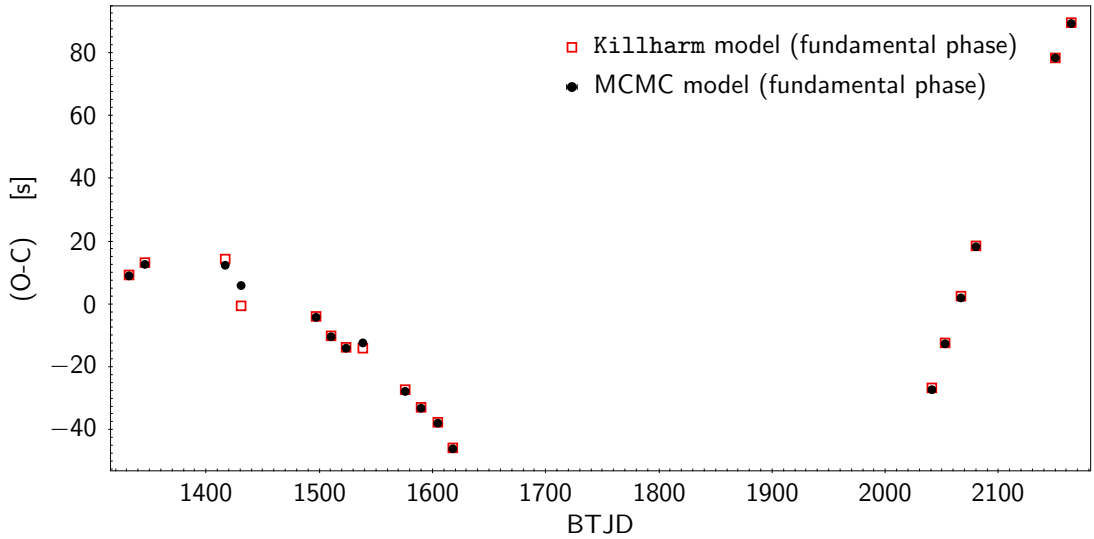

Figure 6.10: Resulting $(O-C)$ diagram of V393 Car. Red squares are returned by simple least-square regression as described in subsection 6.1.3, black dots with errorbars are the result of the MCMC fits as described in subsection 6.1.4.

The $(O-C)$ diagram shows phase shifts (in seconds) as the difference between observed fundamental phases, derived from the harmonic analysis I carried out on TESS light curves of V393 Car, and the expected phases, corresponding to the mean computed values, as a function of time in BTJD. The computed error bars are pretty small, namely of the order of $\sim 1/10$ second, reason why are not clearly visible within the diagram. In the figure above (Fig. 6.10) are shown 18 data points corresponding to two points for each TESS light curve, i.e. two points every observing sector (9 in case of V393 Car), one point for orbital segment (∼two weeks). The distribution of phase shifts within the residuals diagram suggests the presence of a sinusoidal periodic signal together with a linear trend. Therefore, this could be an hint of LTEs induced by a secondary body perturbing V393 Car. I will discuss the origin of the LTEs and the nature of the perturber in Chapter 7.

6.2.3 Chang 349

Chang 349 (TIC 260654645) is an HADS having an estimated mass of 1.78 ± 0.16 $M_{\odot}$[7]. Its TESS magnitude is 12.44 (therefore lying on the faint side of our sample) and it was observed in 17 partially consecutive TESS sectors (1-13, 28-31) from 2018 until 2020 (Year 1, 2 and partially Year 3 of the mission). Chang 349 was re-observed in sectors 32 (19 November 2020 to 17 December 2020), 33 (17

[7]See Chapter 5.

December 2020 to 13 January 2021), 34 (13 January 2021 to 9 February 2021), 35 (9 February 2021 to 7 March 2021), 36 (7 March 2021 to 2 April 2021), 37 (2 April 2021 to 28 April 2021), 38 (28 April 2021 to 26 May 2021) and in sector 39 (26 May 2021 to 24 June 2021). I did not included the latter eight sectors in my analysis since those light curves were not available for download when I started the harmonic analysis. Looking at the forthcoming sectors (up to sector 55, 5 August 2022 to 1 September 2022), Chang 349 could be re-observed[8].
The frequency pattern shows one dominant series of frequencies and three other frequencies "combs" whose harmonics are not visible within the spectrum. The other peaks are aliases, i.e. false frequencies contaminating the periodogram typically caused by temporal gaps in observations.

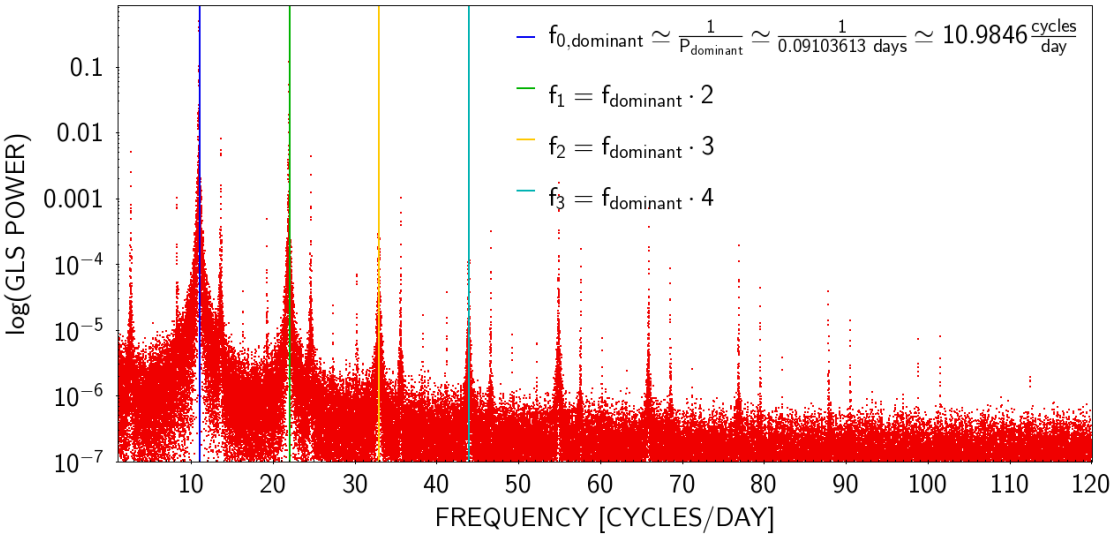

Figure 6.11: GLS Periodogram of Chang 349. The blue vertical line highlights the most dominant frequency within the diagram and the following coloured vertical lines indicates first three equally-spaced harmonics.

The strongest peak in the GLS periodogram corresponds to a dominant pulsation period of $\simeq$ 0.09104 days $\simeq$ 2.2 hours or equivalently to a frequency of $\simeq$ 11 cycles/day. Also in this last case, a pulsation period resulting in a few hours is fully consistent with oscillating properties of HADS stars. The harmonics of the dominant series (colored vertical lines in the periodogram) are integer multiples of the estimated fundamental pulsation frequency. Other peaks do not constitute frequency series but they are only aliases with the dominant period, indeed they

[8]Informations about the scheduled observations available at https://heasarc.gsfc.nasa.gov/cgi-bin/tess/webtess/wtv.py?Entry=TIC+260654645

are equally-spaced.
In the case of Chang 349 I report the resulting $(O - C)$ diagram showing only phase shifts obtained by the MCMC analysis (see subsection 6.1.4) because, by analyzing Chang 134 and V393 Car, it resulted to be preferable compared to a simpler least-squares regression (see subsection 6.1.3).

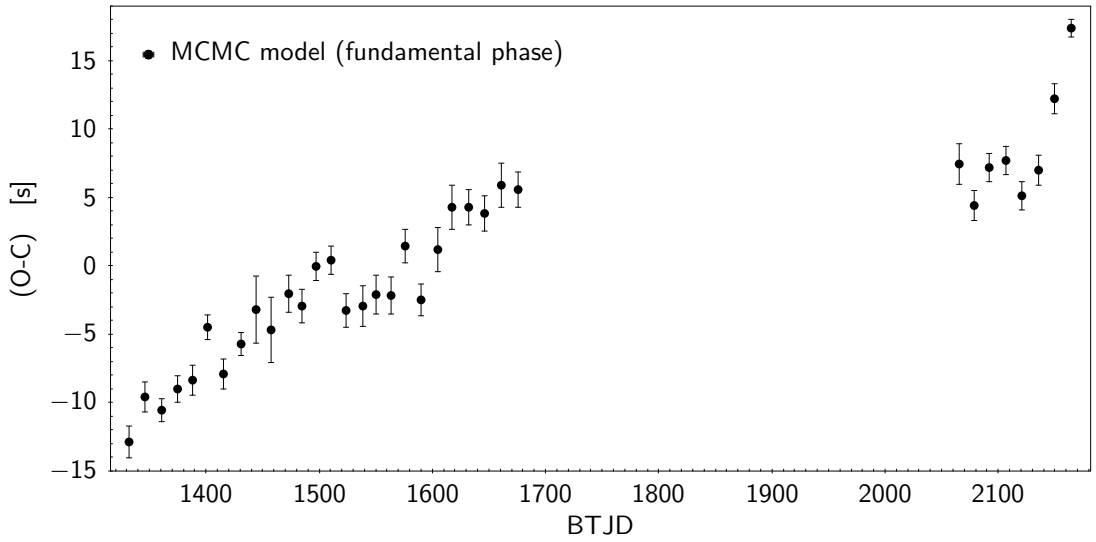

Figure 6.12: Resulting $(O - C)$ diagram of Chang 349. Black dots with error bars are the result of the MCMC fits as described in subsection 6.1.4.

The $(O-C)$ diagram, where phase shifts have been converted to seconds, shows the difference between observed phases derived from the harmonic analysis I carried out on TESS light curves of Chang 349, and the expected phases, corresponding to the mean computed values, as a function of time in BTJD. In the figure above (Fig. 6.12) are shown 34 data points corresponding to two points for each TESS light curve, i.e. two points every observing sector (17 in case of Chang 349), one point for orbital segment (∼two weeks). The two clusters of data show different slopes but any periodic sinusoidal trend is appreciable from the distribution of phase shifts within the $(O - C)$ diagram. This condition implies that I need more observations to clarify the question. The slopes in the diagram have not any physical meaning, they depend only on assumptions on the mean pulsation period. Therefore, observed phase shifts could be an hint of LTEs induced by a secondary body perturbing Chang 349. I will discuss the origin of the LTEs and the nature of the possible perturber in Chapter 7.

6.3 Computation of the expected LTE signal

Before performing the final regression of the $(O-C)$ diagrams, I computed, for each of the three HADS targets selected for my pilot study, the expected semi-amplitude of the LTE as a function of the orbital period and semi-major axis of the external body for different types of perturbers, i.e. from stellar to planetary companions. This preliminary study would give an idea of which portion of the parameter space I am able to investigate exploiting the PT technique just as I implemented it, once known the precision thanks to which I measure the phase shifts. Especially, this pilot investigation would reveal which range of masses (i.e. from stellar companions down to planetary masses), orbital period and semi-major axis is consistent with measured LTEs.

As a first step, I assumed a range of masses for each companion according to Table 2 published by Stevens and Gaudi, 2013. Afterwards, I assumed as mass of the hypotetical perturber in our calculation the mean value computed within each bin.
The table below (Table 6.1) shows mass intervals based on Stevens and Gaudi, 2013 (second column) and the mean computed masses of the perturbers reported in Earth masses unit (third column).

Table 6.1: Assumed masses of the perturbers

Perturber	Mass Range	Mean Mass [$M_\oplus$]
Earth-like	0.1 $M_\oplus$ − 2 $M_\oplus$	1.0
Super Earth-like	2 $M_\oplus$ − 10 $M_\oplus$	6.0
Neptune-like	10 $M_\oplus$ − 100 $M_\oplus$	55.0
Jupiter-like	100 $M_\oplus$ − 10^3 $M_\oplus$	550.0
Brown Dwarf-like	13 M_J − 0.07 $M_\odot$	13722.45
Solar-like	1 $M_\odot$	333030.0

As a second step, I considered equation 2.1[9] and, by fixing the inclination of the orbital plane, i, at $\pi/2$ such that $\sin(i = \pi/2) = 1$, I used the aforementioned equation to compute the semi-amplitude of the expected LTE signal, A, expressed in seconds, as a function of the semi-major axis, a, in the interval from zero to 10 AU, chosen according to the difficulty of sampling efficiently longer orbital periods using present-day techniques. I calculated the respective orbital periods in days according to the third Kepler's law:

[9] In the case of circular orbits: $A \simeq \frac{a \sin(i)}{c} \frac{m_p}{M_\star}$

$$P_{\rm orb} = 2\pi a \cdot \sqrt{\frac{a}{GM_\star}}, \tag{6.12}$$

where $G = 8.88 \cdot 10^{-10} AU^3/M_\oplus \text{days}^2$ is the gravitational constant reported in appropriate units, a is the semi-major axis changing at steps of 0.1 AU in the given range and $M_\star$ is the stellar mass in Earth masses. The masses of Chang 134, V393 Car and Chang 349 I assumed are the ones I computed according to Moya et al., 2018 and Queiroz, Anders, Chiappini et al., 2020. Details about empirical estimation of the mass of the three HADS can be found in Chapter 5.

In the following subsections I report results obtained for the three HADS: Chang 134, V393 Car and Chang 349.
The third column of tables 6.2 , 6.3 and 6.4 shows the computed semi-amplitude of the LTE multiplied by the semi-major axis in the case of different perturbers whose assumed masses are equal to the means computed in Table 6.1. For example, assuming a semi-major axis equal to 2 AU, a Neptune-like exoplanet orbiting Chang 134 would induce an LTE with a semi-amplitude of $0.0598 \cdot 2 \simeq 0.12$ s and a corresponding orbital period of $\simeq 880.3$ days.
The graphics shown represent A as a function of orbital semi-major axis (Fig. 6.13, 6.15 and 6.17) and period (Fig. 6.14, 6.16 and 6.18) of each companion orbiting the three HADS.

6.3.1 Chang 134

Table 6.2: Chang 134, $A(a)$ with a ranging between 0 and 10 AU.

Perturber	M [$M_\oplus$]	$A(a)$ [AU·s]
Earth-like	1.0	0.00109·a
Super Earth-like	6.0	0.00652·a
Neptune-like	55.0	0.05977·a
Jupiter-like	550.0	0.59765·a
Brown Dwarf-like	13722.5	14.9114·a
Solar-like	333030.0	361.885·a

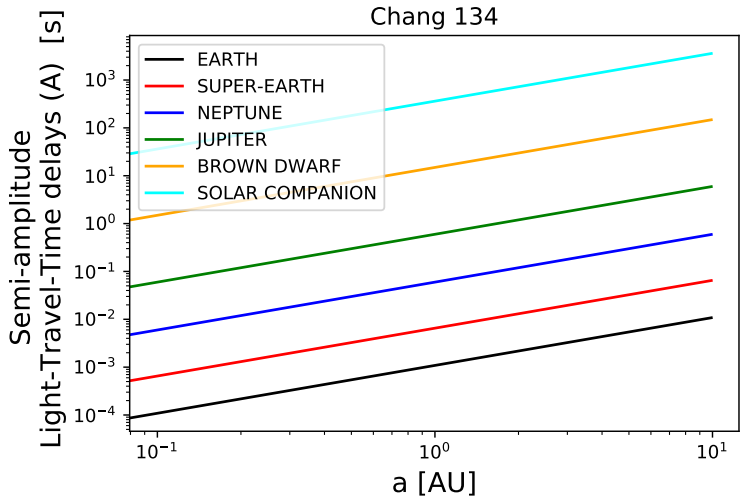

Figure 6.13: Semi-amplitude of the LTE as a function of the orbital semi-major axis varying in the interval 0-10 AU, both axis are in logarithmic scales. Each color refers to a different companion orbiting Chang 134.

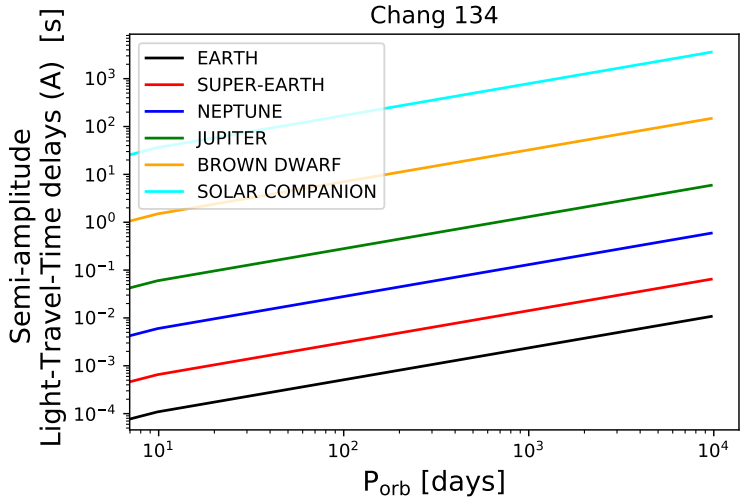

Figure 6.14: Semi-amplitude of the LTE as a function of the orbital period assuming a semi-major axis varying in the interval 0-10 AU, both axis are in logarithmic scales. Each color refers to a different companion orbiting Chang 134.

6.3.2 V393 Car

Table 6.3: V393 Car, $A(a)$ with a ranging between 0 and 10 AU.

Perturber	M [$M_\oplus$]	$A(a)$ [AU·s]
Earth-like	1.0	0.00076·a
Super Earth-like	6.0	0.00455·a
Neptune-like	55.0	0.04167·a
Jupiter-like	550.0	0.41665·a
Brown Dwarf-like	13722.5	10.3955·a
Solar-like	333030.0	252.288·a

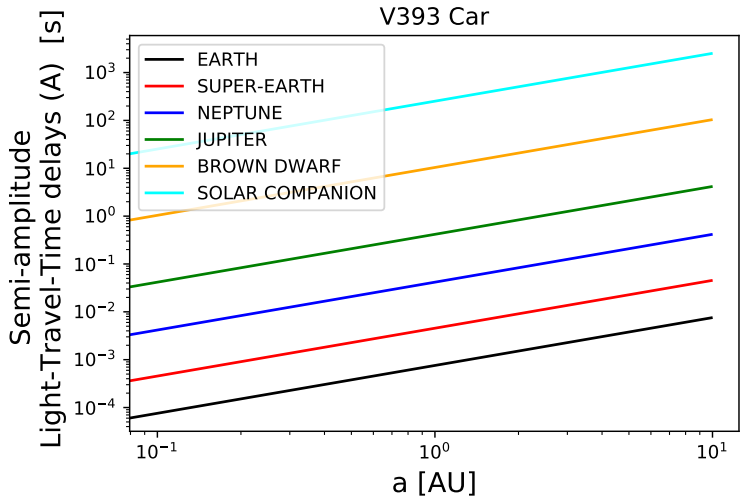

Figure 6.15: Semi-amplitude of the LTE as a function of the orbital semi-major axis varying in the interval 0-10 AU, both axis are in logarithmic scales. Each color refers to a different companion orbiting V393 Car.

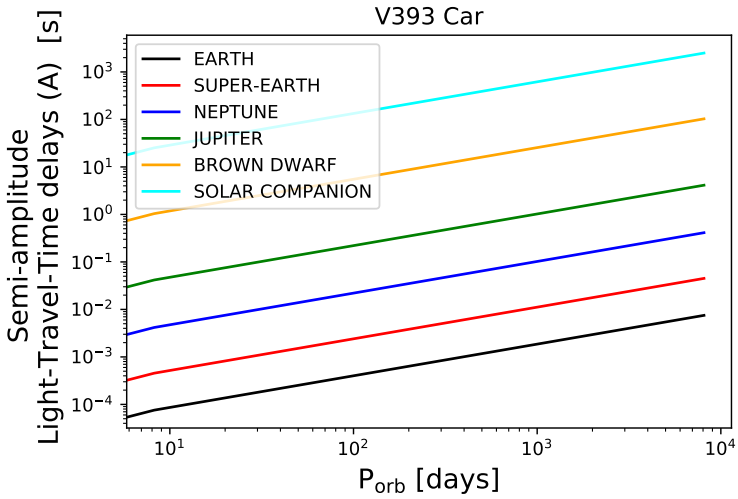

Figure 6.16: Semi-amplitude of the LTE as a function of the orbital period assuming a semi-major axis varying in the interval 0-10 AU, both axis are in logarithmic scales. Each color refers to a different companion orbiting V393 Car.

6.3.3 Chang 349

Table 6.4: Chang 349, $A(a)$ with a ranging between 0 and 10 AU.

Perturber	M [$M_\oplus$]	$A(a)$ [AU·s]
Earth-like	1.0	0.00084·a
Super Earth-like	6.0	0.00506·a
Neptune-like	55.0	0.04634·a
Jupiter-like	550.0	0.46344·a
Brown Dwarf-like	13722.5	11.5628·a
Solar-like	333030.0	280.617·a

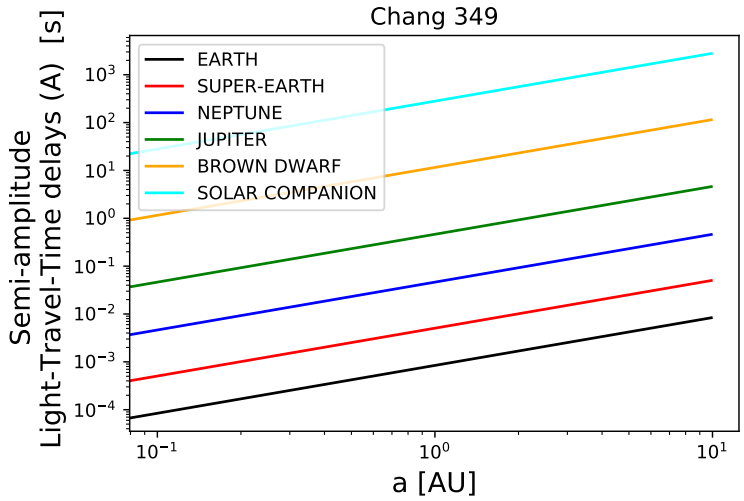

Figure 6.17: Semi-amplitude of the LTE as a function of the orbital semi-major axis varying in the interval 0-10 AU, both axis are in logarithmic scales. Each color refers to a different companion orbiting Chang 349.

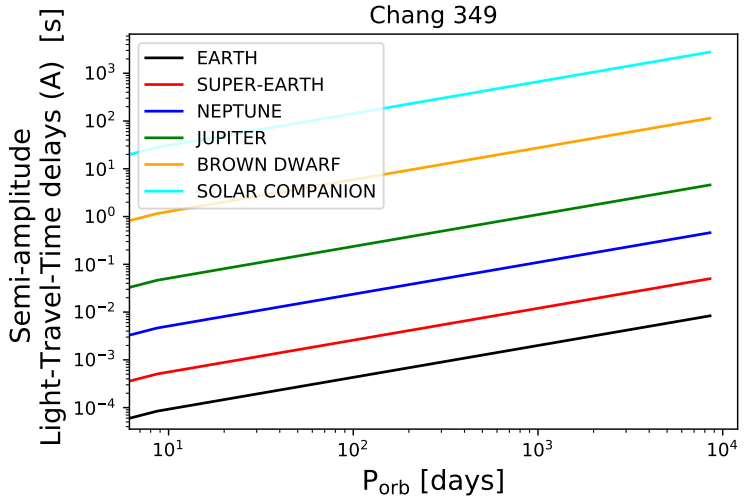

Figure 6.18: Semi-amplitude of the LTE as a function of the orbital period assuming a semi-major axis varying in the interval 0-10 AU, both axis are in logarithmic scales. Each color refers to a different companion orbiting Chang 349.

6.3.4 General discussion

As theoretically predicted by equation 2.1 for simple circular orbits, the more massive the perturber is, and the wider the star-perturber separation is (i.e. large orbital period and semi-major axis), the larger will be the LTE signature. In this context, the challenge of the PT technique is double:

- Even though the method is more sensitive to companions orbiting further from the star, the complete sampling of long orbital periods[10], i.e. long observational baselines, could not be easy from a photometric point of view because it might require observations of the order of tens of years; (for comparison, in the case of perturber-star[11] separations $\sim$ 5 AU the required baseline is $\sim$ 10 yr).
- Moreover, the less massive the perturber is, the smaller the LTE signature is. Therefore, in case of planets having smaller masses such as rocky Earth- and Super-Earth-like exoplanets, the semi-amplitude of the LTE could reach fractions of second at best. For example, a Super-Earth (mass of the order of few Earth masses) orbiting V393 Car at 1 AU induces an LTE with a semi-amplitude of $\simeq 0.0046$ s. For this reason, the signal could be unfeasible to detect because it might be hindered or distorted by systematic errors or issues with the absolute time calibration discussed in section 7.2.

One of the advantages that makes the PT an important technique for searching and characterizing exoplanets is the capability of revealing perturbers at a large separation from the host star. As described in Chapter 1, RV and transit detection methods are not optimized for discovering exoplanets orbiting at wide distances from their hosting star. Therefore, since the PT technique is more sensitive for detecting distant planets, it results in being a unique method to detect exoplanets in larger orbits as well as astrometry.

[10] I need to sample the entire orbital period to infer both the phase and the amplitude.
[11] Considering δSct stars having a mass in the range 1-2 $M_{\odot}$.

Chapter 7
Conclusions

In this final chapter, I present and discuss my attempts at fitting an LTE model to my $(O-C)$ diagrams, in order to infer or constrain the mass and semi-major axis of the perturber for each of the analyzed systems. Furthermore, I discuss issues on TESS timing accuracy, final comments and future developments.

7.1 LTE fit of the (O-C) diagrams

Before performing the actual fit of an LTE model to the $(O-C)$ diagram, I computed a GLS periodogram (see subsection 6.1.2 for details) to search for any significant periodicity in it. I chose this approach because the MCMC optimization I used needs a starting point to converge to a reliable solution, and visually guessing the period does not always lead to the best-fitting solution.
Once a candidate period is found, I run the same MCMC algorithm described in subsection 6.1.4 to fit the simplest possible LTE model (that is, with a circular orbit $e = 0$ corresponding to a sinusoidal function[1]) to my $(O-C)$ diagrams. Lastly, I used the period, the amplitude and corresponding errors returned by the fit to compute both the orbital semi-major axis[2] (in AU) and the mass (in Earth masses) of the perturber according to the following equations:

$$a = \left(\frac{P_{\rm orb}^2 \cdot G \cdot M_\star}{4\pi^2} \right)^{1/3}, \tag{7.1}$$

where $G = 8.88 \cdot 10^{-10} AU^3/M_\oplus$ days^2 is the gravitational constant in appropriate units, $P_{\rm orb}$ is the orbital period in days and $M_\star$ is the stellar mass in Earth masses; and:

$$M_{\rm p} = c \cdot \frac{M_\star \cdot A}{a}, \tag{7.2}$$

where c is the speed of light in AU/s, $M_\star$ is the stellar mass in Earth masses, a is the orbital semi-major axis estimated by equation 7.1 and A is the amplitude

[1] See equations 2.1 and 2.3.
[2] From the third Kepler's law.

computed by the model regression. Since I assumed the orbital inclination angle[3] $i = \pi/2$, the estimated mass coincides with the true mass of the external body. I propagated the uncertainties on both semi-major axis and mass as the quadratic sum of the partial derivatives considering errors on orbital period and amplitude returned by the fit.

Below I show results obtained for the three HADS: Chang 134, V393 Car and Chang 349.

7.1.1 Chang 134

As described in the introduction of section 7.1, as a first step I derived a GLS periodogram to search for a periodicity in the $(O - C)$ diagram of Chang 134 resulting from the harmonic analysis illustrated in Chapter 6 (Fig. 6.8). The period returned by the GLS suggests an orbital period of the external body of 81.75 days (Fig. 7.1).

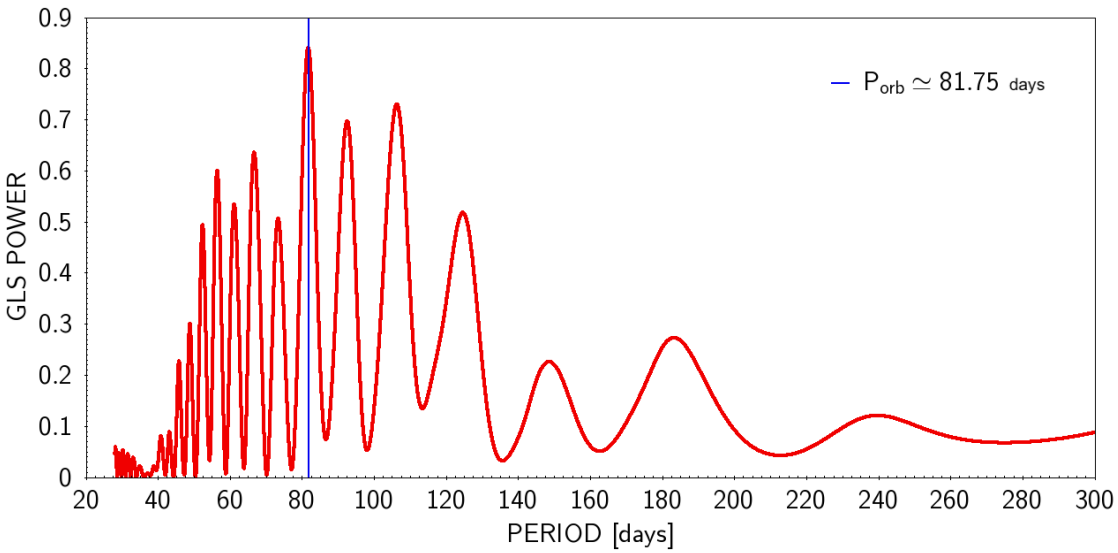

Figure 7.1: GLS Periodogram carried out onto the $(O-C)$ diagram of Chang 134 (Fig. 6.8). The blue vertical line highlights the peak having the highest power corresponding to an orbital period of $\simeq$ 82 days found within the $(O-C)$ diagram of Chang 134.

Afterwards, I performed an MCMC fit to model the $(O-C)$ diagram of Chang 134 (Fig. 6.8). The function adopted as potential best-fit model is the combination of a sinusoidal and a parabolic trend having six free parameters in the fit:

[3] $\sin(i)$=1

$$\mathrm{NL(t)} = b_0 + b_1 \cdot (t - t_{\mathrm{median}}) + b_2 \cdot (t - t_{\mathrm{median}})^2 + A_0 \cdot \cos\left(\frac{2\pi t}{P_{\mathrm{orb}}} + 2\pi\phi_0\right), \quad (7.3)$$

where b_0, b_1 and b_2 are the coefficients of the parabola; A_0 is the amplitude of LTE considering the fundamental frequency; ϕ_0 is the phase and P_{orb} is the orbital period left free to vary starting from the period extracted from the GLS periodogram performed on the $(O - C)$ diagram. After checking the convergence of the MCMC chains, in the following table (Tab. 7.1) are listed the best-fit values with their corresponding uncertainties returned by the final regression of the $(O - C)$ diagram of Chang 134.

Parameter	Best-fit value $\pm$ σ
b_0	-0.26 ± 1.91
b_1	-0.003 ± 0.006
b_2	$(1.17 \pm 1.89) \cdot 10^{-5}$
P_{orb}	81.76 ± 0.28 days
ϕ_0	0.16 ± 0.07
A_0	6.87 ± 0.69 s

Table 7.1: Best-fit parameters returned by the final regression of the $(O - C)$ diagram of Chang 134.

The resulting chi-squared is $\chi^2 = 34.83$ and the respective reduced chi-squared is $\chi^2_{\mathrm{red}} = \chi^2/DOF \simeq 3.5$, where $DOF = 16 - 6 = 10$ are the degrees of freedom of the system, i.e. the number of points of the $(O-C)$ diagram minus the number of free parameters. As a conclusion, the proposed function (Eq. 7.3) is appropriate to model the $(O - C)$ diagram, hence I explained the $\chi^2_{\mathrm{red}} > 1$ as a consequence of uncertainties underestimated by a factor $\sqrt{\chi^2} \simeq 1.9$, supposing random, independent errors and the model linear in its parameters.
It is to be noticed that the orbital period derived by the best-fit model is fully consistent with the value computed by the GLS periodogram.

Below, I report the resulting $(O-C)$ plot fitted according to the model in equation 7.3 (Fig. 7.2).

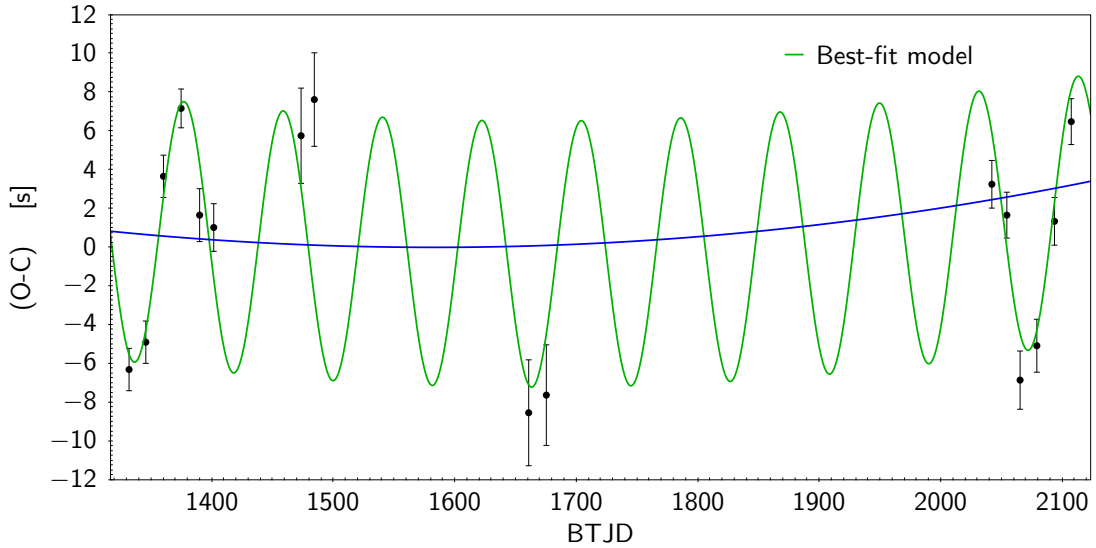

Figure 7.2: Best-fit of the $(O-C)$ diagram of Chang 134. The green model is the resulting best-fit one described by equation 7.3. The blue curve illustrates the parabolic baseline included in the best-fit function. Black dots with error bars are returned by the MCMC approach adopted for the harmonic analysis (see subsection 6.1.4).

Having obtained the best-fit parameters, especially the amplitude and the period, I estimated the orbital semi-major axis and the mass of the perturber according to equations 7.1 and 7.2. As a result I obtained: $a = 0.4101 \pm 0.0032$ AU and $M_{\rm p} = 15400 \pm 1600\ M_{\oplus} \simeq 49 \pm 5\ M_{\rm J}$.
According to the pilot study I made on the expected LTEs induced by different perturbers on varying of mass, orbital period and semi-major axis (described in details in section 6.3), my analysis of Chang 134 are consistent with a brown dwarf companion on a 2.7-months orbit.

7.1.2 V393 Car

At first, I searched for a periodicity in the $(O-C)$ diagram of V393 Car resulting from the harmonic analysis illustrated in Chapter 6 by exploiting the GLS periodogram. Unlike Chang 134, in the case of V393 Car the GLS periodogram did not find a dominant and evident periodicity in the O-C diagram. Hence, the GLS analysis is not conclusive.
Afterwards, I performed an MCMC algorithm to model the $(O-C)$ diagram of V393 Car (Fig. 6.10). The best-fit function I assumed consists in a linear trend added to a sinusoidal one for a total of five free parameters in the fit:

$$\mathrm{NL(t)} = b_0 + b_1 \cdot (t - t_{\mathrm{median}}) + A_0 \cdot \cos\left(\frac{2\pi t}{P_{\mathrm{orb}}} + 2\pi\phi_0\right), \tag{7.4}$$

where b_0 and b_1 are the coefficients of the straight line, namely the vertical offset and the angular coefficient; A_0 is the amplitude of LTE considering the fundamental frequency; ϕ_0 is the phase and P_{orb} is the orbital period. Since the orbital period of the perturber cannot be extracted from the periodogram, I derived it by imposing it as a free parameter returned by the regression.
After checking the convergence of the MCMC chains, in the following table (Tab. 7.2) are listed the best-fit values with their uncertainties returned by the final regression of the $(O - C)$ diagram of V393 Car.

Parameter	Best-fit value $\pm$ σ
b_0	-44.6 ± 0.3
b_1	0.270 ± 0.004
P_{orb}	1150.1 ± 5.5 days
ϕ_0	0.849 ± 0.007
A_0	126.3 ± 1.2 s

Table 7.2: Best-fit parameters returned by the final regression of the $(O - C)$ diagram of V393 Car.

The resulting chi-squared is $\chi^2 = 9830.8$ and the respective reduced chi-squared is $\chi^2_{\mathrm{red}} = \chi^2/DOF \simeq 756.2$, where $DOF = 18 - 5 = 13$ are the degrees of freedom of the system, i.e. the number of points of the $(O - C)$ diagram minus the number of free parameters. As a conclusion, the proposed function (Eq. 7.4) is clearly appropriate to model the $(O - C)$ diagram, hence I explained the $\chi^2_{\mathrm{red}} \gg 1$ as a consequence of uncertainties underestimated by a factor $\sqrt{\chi^2} \simeq 99.2$, supposing random, independent errors and the model linear in its parameters. Indeed, the computed error bars on phase shifts are of the order of 0.1 s.

Below, I report the resulting $(O-C)$ plot fitted according to the model in equation 7.4 (Fig. 7.3).

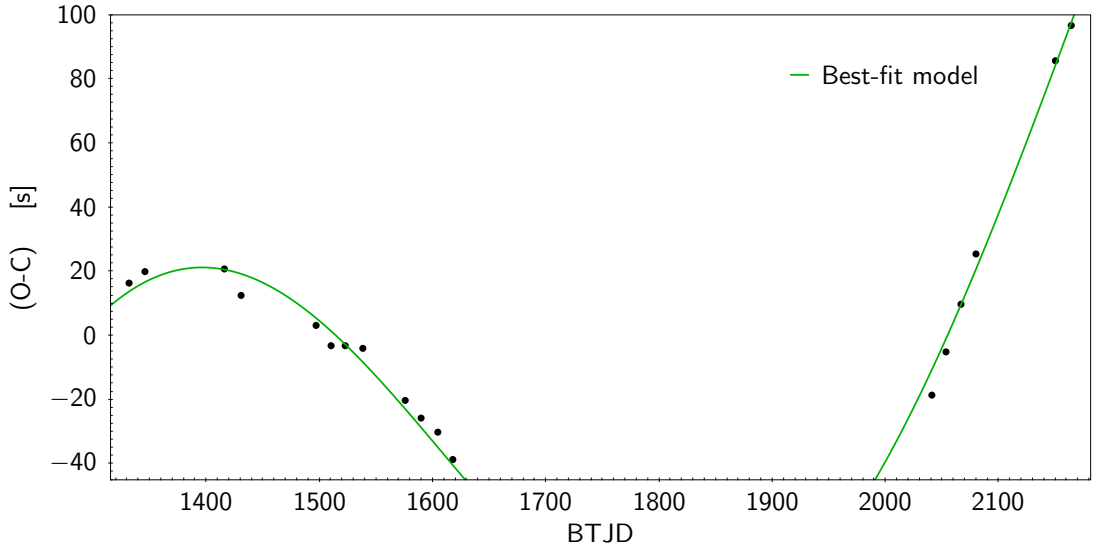

Figure 7.3: Best-fit of the $(O-C)$ diagram of V393 Car. The green model is the resulting best-fit one described by equation 7.4. Black dots with error bars are returned by the MCMC approach adopted for the harmonic analysis (see subsection 6.1.4).

Having obtained the best-fit parameters, especially the amplitude and the period, I estimated the orbital semi-major axis and the mass of the perturber according to equations 7.1 and 7.2. As a result I obtained: $a = 2.70 \pm 0.08$ AU and $M_{\rm p} = 61900 \pm 5700\ M_{\oplus} \simeq 195 \pm 18\ M_{\rm J}$.
According to the pilot study I made on expected LTEs induced by different perturbers on varying of orbital period and semi-major axis (described in details in section 6.3), my analysis of V393 Car are consistent with an M-dwarf companion on a 3.2-years orbit.

7.1.3 Chang 349

As a first step, I searched for a periodicity in the $(O-C)$ diagram of Chang 349 resulting from the harmonic analysis illustrated in Chapter 6 by exploiting the GLS periodogram. Unlike Chang 134, in the case of Chang 349 the GLS periodogram did not find a dominant and evident periodicity in the distribution of the phase shifts within the $(O-C)$ diagram (Fig. 6.12). Hence, the GLS is not conclusive because it returned three potential orbital periods but none of them provided a reasonable solution (see Fig. 7.4).

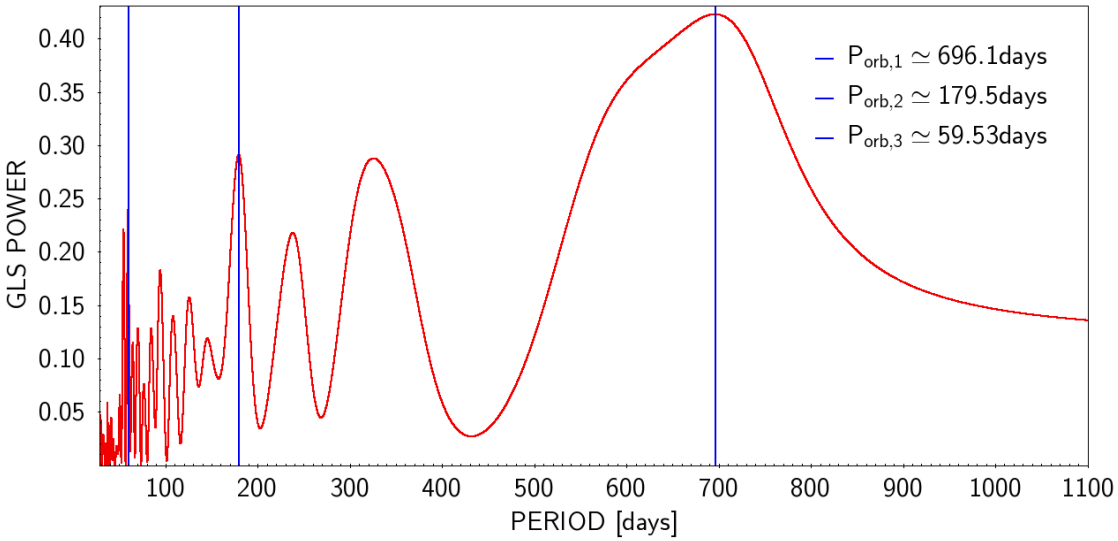

Figure 7.4: GLS Periodogram carried out onto the $(O-C)$ diagram of Chang 349 (Fig. 6.12). The blue vertical lines highlight the peaks having the highest power corresponding to three possible orbital periods inferred by the $(O-C)$ diagram of Chang 349.

The $(O-C)$ diagram of Chang 349 resulting from the harmonic analysis illustrated previously exhibits two clusters of data both following a linear trend but showing two different slopes. It is appreciable a significant variation of phases as the time varies, however, by subtracting the linear trends, the data distribution cannot be modelled by a sinusoidal shape and the three periods obtained from the GLS did not provide a convincing solution.

Below, I report the $(O-C)$ diagram of Chang 349 once I removed the linear trends (Fig. 7.5).

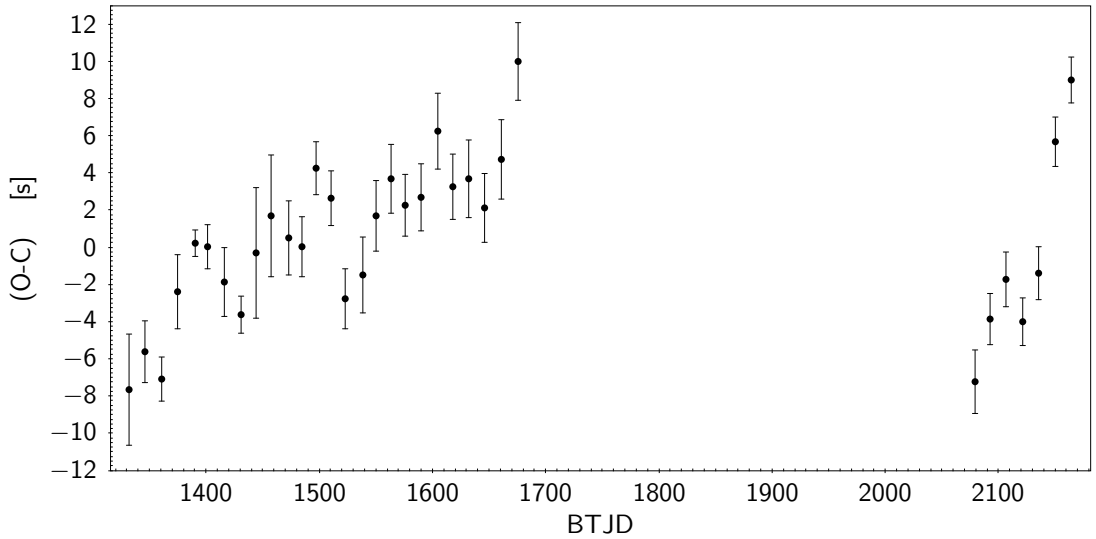

Figure 7.5: $(O - C)$ diagram Chang 349 after I removed the linear trends. Black dots with error bars are returned by the MCMC approach adopted for the harmonic analysis (see subsection 6.1.4).

Therefore, I conclude that the analysis carried out for Chang 349 is not conclusive because, by fitting the $(O - C)$ diagram, no sinusoidal trend is able to explain the behavior of the system. Since I did not infer any sinusoidal shape, neither the semi-amplitude nor the orbital period could be derived; as a consequence, I cannot speculate on which type of unseen companion might perturb Chang 349, it remains an open question and I need more data, i.e. observations, to obtain more hints about the nature of the system.

7.2 TESS timing accuracy

During my work, I encountered some limiting factors preventing me to achieve the theoretical sub-second sensitivity for the LTE detection. One of the most crucial issues is the uncertainty on the absolute calibration of the TESS time stamps, which are known to show drifts up to a few seconds with a different behavior on different sectors, as documented by the TESS Science Processing Operations Center (SPOC) in official data release notes (DRN)[4].

Aforementioned issues might be due to constant drifts of the internal clock on-board TESS which is accurate in its own time but with respect to the universal coordinated time (UTC) it shows drifts and offsets possibly caused by additional

[4] https://archive.stsci.edu/tess/tess_drn.html

readout offsets of TESS cameras, hardware limitations, electronics and data downlinks. Unless these systematics are not properly modeled and corrected to recalibrate TESS time stamps, it is possible for a genuine planetary LTE to be hindered or distorted by them, compromising the goal of discovering exoplanets especially those having smaller masses.

Before TESS became operative in 2018, Hans Kjeldsen, Jørgen Christensen-Dalsgaard and Bill Chaplin in 2013/2014 published a document summarizing the TESS timing requirements for asteroseismology (SAC/TESS/0002)[5]. TESS timing requirements are fundamental in the case of high-amplitude coherent oscillators like RR-Lyrae and δSct stars, especially HADS which are the primary targets of my master thesis project.
According to the study carried out by Montgomery and Odonoghue, 1999, Kjeldsen and collaborators computed the accuracy of the pulsation phase as:

$$\sigma(\phi) = \sqrt{\frac{2}{N}} \cdot \frac{\sigma(\mathrm{m})}{A}, \tag{7.5}$$

where N is the total number of data, $\sigma(m)$ is the relative scatter per measurement i.e. the mean error associated to the N measurements and A is the amplitude of the oscillation. The corresponding accuracy of the internal clock of TESS spacecraft to obtain a stable phase is:

$$\sigma(\mathrm{time}) = \sqrt{\frac{2}{N}} \cdot \frac{\sigma(\mathrm{m})}{A} \cdot \frac{P_{\mathrm{dominant}}}{2\pi}, \tag{7.6}$$

where P_{dominant} is the dominant pulsation period. This corresponds also, neglecting systematic errors, to the timing precision expected while observing a sinusoidal pulsator with these characteristics.

I estimated both quantities for the three pilot targets: Chang 134, V393 Car and Chang 349. Results are summarized in the table below (Tab. 7.3).

[5] https://tasoc.dk/info/docs.php

Table 7.3: Accuracy of the pulsation phase and accuracy of the on-board clock computed for the three HADS stars according to results of the harmonic analysis (see Chapter 6) and to equations 7.5 and 7.6.

HADS	$P_{\text{dom.}}$ [days]	N	σ(m)	A [s]	$\sigma(\phi)$	σ(time) [s]
Chang 134	0.1294	7997.75	$4.22{\cdot}10^{-3}$	0.09	$7.56{\cdot}10^{-4}$	1.35
V393 Car	0.1413	7767.39	$2.65{\cdot}10^{-4}$	0.06	$6.96{\cdot}10^{-5}$	0.14
Chang 349	0.0910	7878.97	$6.68{\cdot}10^{-3}$	0.11	$9.89{\cdot}10^{-4}$	1.24

P_{dominant} is the dominant pulsation period derived by the GLS periodogram. For A I assumed the mean amplitude derived by the non-linear model fitting the light curve. N is the number of points within each orbit of the light curve and it is given by the ratio between the total number of rows of the output file containing all orbital segments of the filtered light curve divided by the number of orbits (i.e. two times the number of observing TESS sectors). σ(m) is the mean photometric error.
The estimated σ(time) for each HADS is the uncertainty with which I am able to reconstruct the arrival time of the stellar signal. The computed values are consistent with error bars on phase shifts in $(O-C)$ diagram derived by the MCMC model (see subsection 6.1.4). Both Chang 134 and Chang 349 have uncertainties of the order of $\sim$ 1 second, promising for future perspectives. Quite the opposite, error bars computed for phase shifts of V393 Car are of the order of $\sim$1/10 of second that could imply difficulties in reaching a sub-second sensitivity without calibrating accurately the satellite.

The main tasks required for TESS timing datasets listed in the document by Kjeldsen and collegues are:

1. (RS-TASC-01) To reach the highest possible TESS photometric quality from 2-min short cadence and to reach the photon noise limit for the brightest stars, the absolute photometry needs to be accurate better than 5 msec, which corresponds to a clock stability of about 0.5 ppm.

2. (RS-TASC-02) Furthermore, to reach the theoretical accuracy of high-amplitude coherent oscillations it is necessary an accurate exposure time better than 5 msec (corresponding to a clock accuracy of 0.002 ppm) over the period of an observing sector which is at least 27 days.

3. (RS-TASC-03) Moreover, always considering coherent pulsation modes, the transformation from the local on-board time to the Heliocentric Julian date (HJD) or barycentric Julian date (BJD) needs to be very accurate with an

accuracy better than 5 msec and this requires to know the telemetry of the spacecraft, i.e. the 3D-position of the satellite at any given time better than 1500 km relative to the Sun. The barycentric correction of the spacecraft is strictly necessary because the barycenter of the Solar System is an inertial reference frame while the Earth is not. Therefore, the motion of the Earth around the Sun induces shifts in the incoming stellar signals which could be moved up or delayed as a consequence, hence, I need to correct it.

4. (RS-TASC-04) Furthermore, in order to compare TESS photometric data together with ground-based photometry, I need to estimate the absolute time of a given photometric data point with respect to a reference point which could be the central time of a given observation; in the case of coherent oscillations, the absolute time in HJD/BJD should be known to better than 0.5 sec. Whereas, in the case of solar-like oscillations, the time should be accurate better than one second over a period of 10 days corresponding to clock accuracy of 1 ppm (RS-TASC-05).

Studying the semi-amplitude of LTEs induced by different types of perturbers (such as planets and/or stellar companions) on varying of the orbital semi-major axis and period of the secondary body (see section 6.3), I observed that, in the case of δSct stars with masses in the range 1.2-2 $M_{\odot}$, only LTEs caused by massive perturbers can be feasibly detected, i.e. Jupiter-like exoplanets and/or stellar companions. Since our ambitious aim is the capability of revealing smaller exoplanets on orbits having more narrow star-planet separations, systematic issues must be corrected to reach the theoretical sub-second sensitivity of the PT in case of perturbers of small mass. For this purpose, the solution I propose is to exploit the global timing properties of an ensemble of bright[6] eclipsing binaries (EBs) to calibrate TESS time stamps by modelling and subtracting systematic drifts and errors, trying to respect timing requirements listed in SAC/TESS/0002. A single EB cannot be considered as a precise astronomical clock because it might show intrinsic LTEs but considering a group of EBs, LTEs should average to zero globally, since they are independent systems whose LTEs (if present) are not correlated. The challenge of this approach is that I need to know ahead of schedule the mean ephemerides of each EB system. Therefore, I have to accurately select a list of targets observed frequently in the last years such that ephemerides are well known. TESS continuos viewing zone (CVZ) objects are preferred. To carry out this selection it is necessary to match observations and results from published literature together with catalogued properties. Two possible starting point catalogues I suggest could be:

[6]E.g. $T < 10$ mag, since TESS is optimized to observe bright stars.

- TIming DAtabase at Krakow (TIDAK[7]) which gathers together $(O-C)$ diagrams and updated linear elements of EB. The database is described in details by Kreiner, 2004.
- The catalogue of the physical properties of well-studied detached eclipsing binaries (DEBCat[8]) based on the list given by Andersen, 1991. The database is described in details by Southworth, 2014.

Once chosen the sample of suitable EBs, two types of calibration of TESS timestamps can be performed:

- A relative calibration, i.e. TESS self-calibration approach, is driven by comparing TESS photometric observations taken in different epochs of the group of EBs carefully chosen. Thanks to this comparison, systematic issues of the satellite could be modelled and subtracted from the observations.
- An absolute calibration described in details in the following subsection 7.2.1.

7.2.1 TESS absolute calibration

To perform an absolute calibration, measurements taken independently from TESS must be borne in mind. In this context, ground-based observations[9], which are reliable from a timing point of view and work as a zero reference point for TESS data sets, are optimal. The analysis carried out in this scenario consists in a cross-correlation between ground- and space-based time series gathered by simultaneous observations of the shortlist of EBs both by TESS and ground-based facilities. In principle, what is done is an $(O-C)$ diagram to compare ground and space data to quantify and model the systematic errors of the satellite.

Robotic and low-cost ground-based telescopes are preferred in this science case. Potential ground-based facilities to take into account for the absolute calibration are:

- The Asiago Schmidt 67/92 cm telescope[10] in Asiago (VI), Italy
- The Rapid Eye Mount 60 cm telescope[11] (REM) located at La Silla observatory in Chile, optimized for visible/infrared observations.
- The two 1.2 m STELLar Activity telescopes[12] (STELLA) located at Tenerife in Spain to monitor activity of cool stars.

[7] https://www.as.up.krakow.pl/ephem/
[8] https://www.astro.keele.ac.uk/jkt/debcat/
[9] The advantage of observing from ground is that the barycentric correction is well known.
[10] https://www.oapd.inaf.it/asiago
[11] http://www.rem.inaf.it
[12] https://www.aip.de/en/research/projects/stella/

- The Stellar Observations Network Group[13] (SONG) made up of a global-spanning ensemble of small telescopes to characterize stellar properties (i.e. asteroseismology) and planetary systems orbiting those stars.

To carry out the absolute calibration of TESS time stamps, one favorable and exemplifying target having very accurate timing from ground-based observations is HW Virginis (HW Vir, Marang and Kilkenny, 1989). HW Vir is an Algol-type, detached EB, made up of a B-type sub-dwarf primary star and an M-dwarf companion (~ 0.25 $M_\odot$, ~ 26000 K and ~ 0.12 $M_\odot$, ~ 4700 K, respectively) exhibiting almost total, very deep and V-shaped eclipses lasting ~ 20 minutes and a short orbital period of a few hours (~ 3 hours). Short duration times and orbital periods allow to detect complete eclipses.
In a recent study published by Esmer et al., 2021, authors estimated an error on mid-eclipse times obtained from ground-based observations (Table A.1) of the order of $10^{-4} - 10^{-5}$ days, i.e. from a few seconds down to $\simeq 0.864$ seconds. Eclipses of HW Vir were observed also with the Asiago ground-based facility by Brown-Sevilla et al., 2021, who combined new eclipse timings with historical photometric observations gathered between 1983 and 2012. The Asiago research group obtained a precision of the order of $\simeq 0.3$ seconds over a single measured primary eclipse timing T_0 (Table 3 of the work).
Therefore, on suitable EBs carefully selected with deep eclipses, possibly V-shaped, short orbital periods and short eclipse duration times (e.g. HW Vir) is demonstrated that it is possible to reach a precision in measurements of the absolute time of mid-eclipses of the order of one tenth of a second.

In 2020, Carolina Von Essen and collaborators (Essen et al., 2020) published a paper focused on TESS timing verification according to requirements reported by the aforementioned official document (SAC/TESS/0002). In particular, authors worked on solving TESS absolute calibration issues exploiting simultaneous observation of a group of EBs almost of Algol-type, showing deep and short eclipses. They performed a cross-correlated analysis between ground-based observations gathered by the 2.15 m Jorge Sahade telescope (CASLEO-2.15) and TESS space-based observations obtaining a time offset equal to $\simeq 5.8$ seconds consistent with TESS measuring the barycentric time ahead of real time. Furthermore, authors evaluated mid-eclipse times of 26 EBs observed exclusively by TESS to search for systematic drifts and to realize a relative calibration. They estimated a timing drift of $\simeq 0.009$ sec/day.
For their work, Carolina Von Essen and collaborators assumed global systematic errors of the satellite neglecting drifts and offsets between sectors as well as between cameras. To refine the calibration considering the mentioned additional

[13] https://phys.au.dk/song/k

drifts/offsets with a different behavior on different sectors and cameras, I suggest to observe at least four different EBs (one for each TESS camera within an observing sector) every month because a sector is covered for $\sim$ 27 days. Since this improvement requires a more complex process of suitable targets selection, a prospective pilot study may consider well-known EBs observed by the fourth camera which points the ecliptic poles towards the CVZ, sky-region with greater observational coverage (see Fig. 7.6). In this manner, it should be necessary one EB observed in the north ecliptic hemisphere for 13 consecutive sectors and another EB in the south ecliptic hemisphere pointed for other 13 consecutive sectors. The advantage of this approach is that one carefully selected system for each hemisphere in enough because such EB is continuously observed for 13 TESS sectors and astronomers do not have to choose several EBs on different sectors. The challenge is that it might be difficult to find known EBs observed uninterruptedly in many sectors by the satellite.

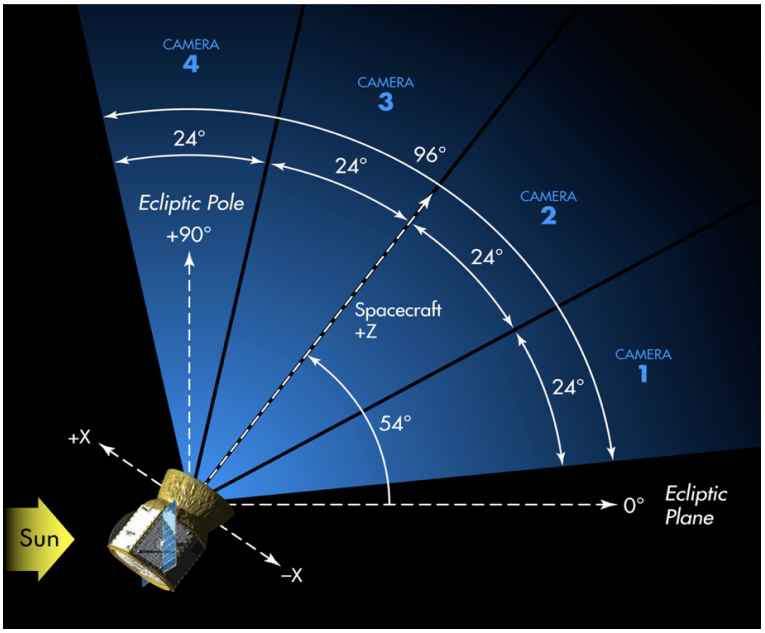

Figure 7.6: Four TESS cameras mapping four different sky-regions. As indicated, camera 1 observes nearby the ecliptic plane whereas camera 4 points the ecliptic pole. Image credit: https://heasarc.gsfc.nasa.gov/docs/tess/primary.html

The previously described empirical approach to calibrate TESS time stamps can be suggested to solve possible calibration issues of the forthcoming M-class ESA

PLATO mission[14] (PLAnetary Transits and Oscillations of stars, Rauer et al., 2014), scheduled to be operative starting from 2026 having as primary science goal the discovery of terrestrial exoplanets (i.e. rocky Earth twins and Super-Earth-like planets) orbiting in the habitable zone of bright[15] Solar-type stars[16]. Indeed, differently from the TESS mission, the PLATO mission is optimized also for carrying out asteroseismological observations, where accurate timing observations are strictly required to construct models describing the internal structure of stars and their age in order to better understand the stellar evolutionary path which influences the planetary formation and evolution.

7.3 Final discussion

The purpose of this thesis is to exploit the PT method to search and characterize exoplanets in orbit around oscillating stars whose pulsation period, intrinsically very coherent, is phase-shifted when a perturbing external body induces the star to orbit around the common barycenter of the system. The resulting effect is called Light Travel Effect or LTE. As theoretically predicted, the more massive the perturber is, and the wider the semi-major axis is, the larger will be the LTE signature by assuming the simple case of circular orbits (null eccentricity).

My work consists in a pioneering analysis of 2-minutes TESS extracted light curves from a sample of suitable HADS carefully selected by cross-matching the catalog published by Chang et al., 2013 together with the CTL of TESS. I shortlisted three HADS stars to apply the PT technique: Chang 134 (M = 1.38±0.03 $M_{\odot}$), V393 Car (M = 1.98±0.17 $M_{\odot}$) and Chang 349 (M = 1.78±0.16 $M_{\odot}$). I derived, for the fundamental pulsation mode, the phase shifts of the stellar signal as a function of time, so called "$(O-C)$" diagram, to search for an LTE caused by an unseen companion able to explain the behavior of the system. I made use of `VARTOOLS` Light Curve Analysis Program to carry out a two-level harmonic analysis by implementing at first a simple least-squares regression and later a more sophisticated Monte Carlo Markov Chain (MCMC) approach to sample the posterior distribution of the best-fit pulsation parameters to estimate uncertainties on $(O-C)$ phases. Afterwards, I retrieved the single-planet, circular LTE model which best fits the $(O-C)$ diagram of each HADS. This latter regression returned the orbital period of the secondary body and the semi-amplitude of the LTE which is directly proportional to the minimum mass of the perturber, to its orbital semi-major axis and inversely proportional to the stellar mass. Having computed the

[14] https://sci.esa.int/web/plato/
[15] V < 11.
[16] F-, G-, K-type stars and bright M-dwarf stars.

stellar masses quoted above according to the works by Moya et al., 2018 and Queiroz, Anders, Chiappini et al., 2020, I calculated the semi-major axis (from the best-fit orbital period) and the mass of the perturber. Lastly, I compared them with my predictions on the expected LTE amplitude as a function of the semi-major axis for different types of companions. From the outcome of my harmonic analysis, and by assuming circular orbits ($e = 0$) and edge-on orbits ($i = \pi/2$) for the LTE modeling, I conclude that the observed $(O - C)$ diagrams could be explained by the presence of a brown dwarf companion of $M_{\rm p} = 15400 \pm 1600\ M_{\oplus} \simeq 49 \pm 5\ M_{\rm J}$ in orbit around Chang 134 at $\simeq 0.4$ AU and an M-dwarf companion having $M_{\rm p} = 61900 \pm 5700\ M_{\oplus} \simeq 195 \pm 18\ M_{\rm J}$ in a $\sim$ 3-year orbit around V393 Car. Quite the opposite, the harmonic analysis carried out for Chang 349 turned out to be not conclusive because no sinusoidal trend is able to model its $(O - C)$ diagram. Therefore, unlike the other two HADS stars, I cannot speculate on a potential unseen companion perturbing the system. It remains an open question and more observations are needed to unveil the nature of the system.

From results obtained thanks to the described exploratory harmonic analysis, I conclude that the PT technique is fruitful in detecting secondary massive companions, i.e. especially stellar masses, in larger orbits. Therefore, PT detection method plays a crucial role when the most employed techniques, as well as transits and radial velocities, fail in characterizing orbital and intrinsic properties of further external bodies.

7.3.1 Outlooks

Since the PT is one of the less explored techniques in exoplanetary astrophysics, it has a large margin for improvement. To this purpose, in the near future, the PT method can be exploited to search for companions in a wider sample of pulsating stars having different spectral types, not necessarily δSct or variables located within instability strip, namely RR-Lyrae and Cepheid variables. Such targets could also be reasonably included within the sample of PLATO objects of interest, increasing both the observational baseline and the photometric precision. Furthermore, during my thesis work I encountered pulsators exhibiting more complex frequency spectra resulting in entwined patterns of pulsation modes (i.e. not pure pulsators such as Chang 134) and/or spectral features like aliases and rotational splitting multiplets. Therefore, starting from my pilot work focused on the simple case of HADS stars for which the PT yields a high S/N, the PT technique can be generalized to new scenarios considering other types of pulsators showing more complex patterns of pulsations, by also addressing issues regarding the aforementioned absolute time calibration of TESS satellite (details in section 7.2). Moreover, the PT model to be fitted can also be generalized by allowing ec-

centric systems, i.e. by searching for secondary external bodies in eccentric orbits ($e \neq 0$), extending my research project to non-standard scenarios.
In the short term, the main source of photometric data will be the TESS mission which continues gathering data and extending the temporal baseline of the observations which is crucial in my science case because moving to LTE signals with larger periods means to improve the sensitivity of the technique to perturbers with smaller masses. For the same goal, TESS data can be complemented with other archival light curves (when available) or with on-purpose observations at ground-based facilities such as the Asiago Observatory.
In conclusion, when the PLATO mission will start releasing data, the synergy between TESS and PLATO will boost the opportunity given by the PT technique by combining gathered observations and by better calibrating mission time stamps.
The analysis of high-precision photometric time series of pulsating stars could also lead to the serendipitous discovery of transiting planets around them. A very small number of planets belonging to this class are so far known and well-characterized, and therefore could be potential follow-up targets for the forthcoming medium class ESA ARIEL mission[17] (Atmospheric Remote-sensing Infrared Exoplanet Large-survey, Pascale et al., 2018) whose launch is planned for 2029. Indeed, ARIEL science objective will be the direct observation of about 1000 hot/warm exoplanets (temperature > 600 K) orbiting M-,F-type stars. The main goal of the mission will be the characterization of the atmosphere of already known planets by exploiting visible/infrared photometry and infrared spectroscopy.

[17] https://arielmission.space

Bibliography

[1] J. Andersen. 'Accurate masses and radii of normal stars'. In: 3.2 (Jan. 1991), pp. 91–126. DOI: 10.1007/BF00873538 (cit. on p. 86).

[2] V. Antoci et al. 'The first view of δ Scuti and γ Doradus stars with the TESS mission'. In: *mnras* 490.3 (Dec. 2019), pp. 4040–4059. DOI: 10.1093/mnras/stz2787. arXiv: 1909.12018 [astro-ph.SR] (cit. on pp. 42, 44).

[3] M. Bailes. 'Millisecond Pulsar Surveys'. In: *IAU Colloq. 160: Pulsars: Problems and Progress*. Ed. by S. Johnston, M. A. Walker and M. Bailes. Vol. 105. Astronomical Society of the Pacific Conference Series. Jan. 1996, p. 3 (cit. on p. 25).

[4] L. A. Balona. 'Possible planets around A stars'. In: *mnras* 441.4 (July 2014), pp. 3543–3549. DOI: 10.1093/mnras/stu822 (cit. on p. 23).

[5] William J. Borucki et al. 'Kepler Planet-Detection Mission: Introduction and First Results'. In: *Science* 327.5968 (Feb. 2010), p. 977. DOI: 10.1126/science.1185402 (cit. on pp. 23, 27, 28, 32).

[6] S. B. Brown-Sevilla et al. 'A new photometric and dynamical study of the eclipsing binary star HW Virginis'. In: (July 2021). DOI: 10.1093/mnras/stab1843. arXiv: 2106.15632 [astro-ph.SR] (cit. on p. 87).

[7] V. M. Canuto. 'The mixing length parameter alpha'. In: 227.1 (Jan. 1990), pp. 282–284 (cit. on p. 22).

[8] S.-W. Chang et al. 'STATISTICAL PROPERTIES OF GALACTIC δ SCUTI STARS: REVISITED'. In: *The Astronomical Journal* 145.5 (Mar. 2013), p. 132. ISSN: 1538-3881. DOI: 10.1088/0004-6256/145/5/132. URL: http://dx.doi.org/10.1088/0004-6256/145/5/132 (cit. on pp. 37, 39, 89).

[9] M. -A. Dupret et al. 'Theoretical instability strips for δ Scuti and γ Doradus stars'. In: 414 (Jan. 2004), pp. L17–L20. DOI: 10.1051/0004-6361:20031740 (cit. on pp. 22, 23).

[10] A. S. Eddington. 'The pulsation theory of Cepheid variables'. In: *The Observatory* 40 (Aug. 1917), pp. 290–293 (cit. on p. 21).

[11] Ekrem M. Esmer et al. 'Revisiting the analysis of HW Virginis eclipse timing data. I. A frequentist data modeling approach and a dynamical stability analysis'. In: 648, A85 (Apr. 2021), A85. DOI: 10.1051/0004-6361/202038640. arXiv: 2103.00062 [astro-ph.SR] (cit. on p. 87).

[12] Carolina von Essen et al. 'TESS Data for Asteroseismology: Timing Verification'. In: *The Astronomical Journal* 160.1 (June 2020), p. 34. ISSN: 1538-3881.

DOI: 10.3847/1538-3881/ab93dd. URL: http://dx.doi.org/10.3847/1538-3881/ab93dd (cit. on p. 87).

[13] M. Gabriel et al. 'Influence of convection on the vibrational stability of stars towards non-radial oscillations.' In: 40.1-2 (Apr. 1975), pp. 33–39 (cit. on p. 22).

[14] Jonathan P. Gardner et al. 'The James Webb Space Telescope'. In: *Space Science Reviews* 123.4 (Nov. 2006), pp. 485–606. ISSN: 1572-9672. DOI: 10.1007/s11214-006-8315-7. URL: http://dx.doi.org/10.1007/s11214-006-8315-7 (cit. on p. 34).

[15] J. A. Guzik et al. 'Driving g-mode Pulsations in Gamma Doradus Variables'. In: *IAU Colloq. 176: The Impact of Large-Scale Surveys on Pulsating Star Research*. Ed. by L. Szabados and D. Kurtz. Vol. 203. Astronomical Society of the Pacific Conference Series. Jan. 2000, pp. 445–446 (cit. on p. 21).

[16] Gerald Handler. 'Asteroseismology'. In: *Planets, Stars and Stellar Systems. Volume 4: Stellar Structure and Evolution*. Ed. by Terry D. Oswalt and Martin A. Barstow. Vol. 4. 2013, p. 207. DOI: 10.1007/978-94-007-5615-1_4 (cit. on p. 22).

[17] J. D. Hartman and G. Á. Bakos. 'VARTOOLS: A program for analyzing astronomical time-series data'. In: *Astronomy and Computing* 17 (Oct. 2016), pp. 1–72. DOI: 10.1016/j.ascom.2016.05.006. arXiv: 1605.06811 [astro-ph.IM] (cit. on pp. 8, 10, 52).

[18] Gregory W. Henry et al. 'A Transiting "51 Peg-like" Planet'. In: 529.1 (Jan. 2000), pp. L41–L44. DOI: 10.1086/312458 (cit. on p. 17).

[19] J. J. Hermes. 'Timing by Stellar Pulsations as an Exoplanet Discovery Method'. In: *Handbook of Exoplanets* (2018), pp. 787–796. DOI: 10.1007/978-3-319-55333-7_6. URL: http://dx.doi.org/10.1007/978-3-319-55333-7_6 (cit. on pp. 25, 26).

[20] Matthew J. Holman and Norman W. Murray. 'The Use of Transit Timing to Detect Terrestrial-Mass Extrasolar Planets'. In: *Science* 307.5713 (Feb. 2005), pp. 1288–1291. DOI: 10.1126/science.1107822. arXiv: astro-ph/0412028 [astro-ph] (cit. on p. 14).

[21] Steve B. Howell et al. 'The K2 Mission: Characterization and Early Results'. In: 126.938 (Apr. 2014), p. 398. DOI: 10.1086/676406. arXiv: 1402.5163 [astro-ph.IM] (cit. on p. 37).

[22] John B. Irwin. 'The Determination of a Light-Time Orbit.' In: 116 (July 1952), p. 211. DOI: 10.1086/145604 (cit. on pp. 27, 28).

[23] S. O. Kepler et al. 'A Detection of the Evolutionary Time Scale of the DA White Dwarf G117-B15A with the Whole Earth Telescope'. In: 378 (Sept. 1991), p. L45. DOI: 10.1086/186138 (cit. on p. 26).

[24] J. M. Kreiner. 'Up-to-Date Linear Elements of Eclipsing Binaries'. In: 54 (June 2004), pp. 207–210 (cit. on p. 86).
[25] D. W. Kurtz. 'Pulsation of Chemically Peculiar and Pre-Main Sequence Stars in the δ Scuti Instability Strip'. In: *Delta Scuti and Related Stars*. Ed. by Michel Breger and Michael Montgomery. Vol. 210. Astronomical Society of the Pacific Conference Series. Jan. 2000, p. 287 (cit. on p. 22).
[26] Yong-Hwa Lee et al. 'Incidence of High-Amplitude δ Scuti-Type Variable Stars'. In: 60 (June 2008), p. 551. DOI: 10.1093/pasj/60.3.551. arXiv: 0805.0062 [astro-ph] (cit. on p. 24).
[27] F. Marang and D. Kilkenny. 'Recent Minima of the Subdwarf Eclipsing Binary BD -7 3477 (=HW Vir)'. In: *Information Bulletin on Variable Stars* 3390 (Oct. 1989), p. 1 (cit. on p. 87).
[28] Michel Mayor and Didier Queloz. 'A Jupiter-mass companion to a solar-type star'. In: 378.6555 (Nov. 1995), pp. 355–359. DOI: 10.1038/378355a0 (cit. on pp. 13, 16).
[29] D. B. McLaughlin. 'Some results of a spectrographic study of the Algol system.' In: 60 (July 1924), pp. 22–31. DOI: 10.1086/142826 (cit. on p. 16).
[30] M. H. Montgomery and D. Odonoghue. 'A derivation of the errors for least squares fitting to time series data'. In: *Delta Scuti Star Newsletter* 13 (July 1999), p. 28 (cit. on p. 83).
[31] Claire Moutou et al. 'CoRoT: Harvest of the exoplanet program'. In: 226.2 (Nov. 2013), pp. 1625–1634. DOI: 10.1016/j.icarus.2013.03.022. arXiv: 1306.0578 [astro-ph.EP] (cit. on pp. 23, 46).
[32] Andy Moya et al. 'Empirical Relations for the Accurate Estimation of Stellar Masses and Radii'. In: 237.2, 21 (Aug. 2018), p. 21. DOI: 10.3847/1538-4365/aacdae. arXiv: 1806.06574 [astro-ph.SR] (cit. on pp. 8, 10, 46–48, 68, 90).
[33] Fergal Mullally et al. 'Spitzer Planet Limits Around the Pulsating White Dwarf GD66'. In: 694.1 (Mar. 2009), pp. 327–331. DOI: 10.1088/0004-637X/694/1/327. arXiv: 0812.2951 [astro-ph] (cit. on pp. 26, 27).
[34] Simon Murphy. 'A Pulsation Review of Delta Scuti and Related Stars'. In: Sept. 2015, pp. 127–162. ISBN: 978-3-319-09416-8. DOI: 10.1007/978-3-319-09417-5_4 (cit. on pp. 22, 24, 46, 49).
[35] Simon J. Murphy, Timothy R. Bedding and Hiromoto Shibahashi. 'A PLANET IN AN 840 DAY ORBIT AROUND A KEPLER MAIN-SEQUENCE A STAR FOUND FROM PHASE MODULATION OF ITS PULSATIONS'. In: *The Astrophysical Journal* 827.1 (Aug. 2016), p. L17. ISSN: 2041-8213. DOI: 10.3847/2041-8205/827/1/l17. URL: http://dx.doi.org/10.3847/2041-8205/827/1/L17 (cit. on p. 28).

[36] Simon J. Murphy, Hiromoto Shibahashi and Timothy R. Bedding. 'Finding binaries from phase modulation of pulsating stars with Kepler - IV. Detection limits and radial velocity verification'. In: *mnras* 461.4 (Oct. 2016), pp. 4215–4226. DOI: 10.1093/mnras/stw1622. arXiv: 1607.07879 [astro-ph.SR] (cit. on p. 28).

[37] Enzo Pascale et al. 'The ARIEL space mission'. In: *Space Telescopes and Instrumentation 2018: Optical, Infrared, and Millimeter Wave*. Ed. by Makenzie Lystrup et al. Vol. 10698. Society of Photo-Optical Instrumentation Engineers (SPIE) Conference Series. July 2018, 106980H. DOI: 10.1117/12.2311838 (cit. on p. 91).

[38] Michael Perryman. *The Exoplanet Handbook*. 2nd ed. Cambridge University Press, 2018. DOI: 10.1017/9781108304160 (cit. on pp. 13, 15, 18, 25).

[39] A. B. A. Queiroz, F. Anders, C. Chiappini et al. 'From the bulge to the outer disc: StarHorse stellar parameters, distances, and extinctions for stars in APOGEE DR16 and other spectroscopic surveys'. In: 638, A76 (June 2020), A76. DOI: 10.1051/0004-6361/201937364. arXiv: 1912.09778 [astro-ph.GA] (cit. on pp. 8, 10, 48, 68, 90).

[40] A. B. A. Queiroz, F. Anders, B. X. Santiago et al. 'StarHorse: a Bayesian tool for determining stellar masses, ages, distances, and extinctions for field stars'. In: *mnras* 476.2 (May 2018), pp. 2556–2583. DOI: 10.1093/mnras/sty330. arXiv: 1710.09970 [astro-ph.IM] (cit. on p. 48).

[41] H. Rauer et al. 'The PLATO 2.0 mission'. In: *Experimental Astronomy* 38.1-2 (Sept. 2014), pp. 249–330. ISSN: 1572-9508. DOI: 10.1007/s10686-014-9383-4. URL: http://dx.doi.org/10.1007/s10686-014-9383-4 (cit. on p. 89).

[42] George R. Ricker et al. 'Transiting Exoplanet Survey Satellite'. In: *Journal of Astronomical Telescopes, Instruments, and Systems* 1.1 (Oct. 2014), p. 014003. ISSN: 2329-4124. DOI: 10.1117/1.jatis.1.1.014003. URL: http://dx.doi.org/10.1117/1.JATIS.1.1.014003 (cit. on pp. 23, 27, 32, 34, 37).

[43] E. Rodriguez, M. J. Lopez-Gonzalez and P. Lopez de Coca. 'VizieR Online Data Catalog: Delta Scuti stars (Rodriguez+, 2000)'. In: *VizieR Online Data Catalog*, J/A+AS/144/469 (Apr. 2000), J/A+AS/144/469 (cit. on p. 37).

[44] R. A. Rossiter. 'On the detection of an effect of rotation during eclipse in the velocity of the brigher component of beta Lyrae, and on the constancy of velocity of this system.' In: 60 (July 1924), pp. 15–21. DOI: 10.1086/142825 (cit. on p. 16).

[45] R Silvotti et al. 'A giant planet orbiting the 'extreme horizontal branch' star V391 Pegasi'. In: *Nature* 449 (Oct. 2007), pp. 189–91. DOI: 10.1038/nature06143 (cit. on p. 29).

[46] Skiff. *VizieR Online Data Catalog: Catalogue of Stellar Spectral Classifications*. 2009 (cit. on p. 38).
[47] John Southworth. *The DEBCat detached eclipsing binary catalogue*. 2014. arXiv: 1411.1219 [astro-ph.SR] (cit. on p. 86).
[48] Joshua S. Speagle. 'A Conceptual Introduction to Markov Chain Monte Carlo Methods'. In: *arXiv e-prints*, arXiv:1909.12313 (Sept. 2019), arXiv:1909.12313. arXiv: 1909.12313 [stat.OT] (cit. on pp. 58, 59).
[49] Keivan G. Stassun et al. 'The Revised TESS Input Catalog and Candidate Target List'. In: 158.4, 138 (Oct. 2019), p. 138. DOI: 10.3847/1538-3881/ab3467. arXiv: 1905.10694 [astro-ph.SR] (cit. on pp. 34, 35).
[50] Daniel J. Stevens and B. Scott Gaudi. 'A Posteriori Transit Probabilities'. In: 125.930 (Aug. 2013), p. 933. DOI: 10.1086/672572. arXiv: 1305.1298 [astro-ph.EP] (cit. on p. 67).
[51] Mark Taylor. *TOPCAT: Working with Data and Working with Users*. 2017. arXiv: 1711.01885 [astro-ph.IM] (cit. on p. 38).
[52] Jacob T. VanderPlas. 'Understanding the Lomb-Scargle Periodogram'. In: 236.1, 16 (May 2018), p. 16. DOI: 10.3847/1538-4365/aab766. arXiv: 1703.09824 [astro-ph.IM] (cit. on p. 54).
[53] V. Vaulato and D. Gandolfi. *Determinazione di masse di pianeti con periodo orbitale molto corto orbitanti attorno a stelle magneticamente attive*. Tech. rep. Dipartimento di Fisica, Università degli Studi di Torino, 2019 (cit. on pp. 16, 19).
[54] A. Wolszczan and D. A. Frail. 'A planetary system around the millisecond pulsar PSR1257 + 12'. In: 355.6356 (Jan. 1992), pp. 145–147. DOI: 10.1038/355145a0 (cit. on p. 13).
[55] Mathias Zechmeister and M. Kürster. *GLS: Generalized Lomb-Scargle periodogram*. July 2018. ascl: 1807.019 (cit. on pp. 26, 55).

Ringraziamenti

Vorrei anzitutto ringraziare il mio relatore, Giampaolo Piotto, e Valerio per la fiducia, per aver avuto tanta pazienza, per avermi guidato in questo appassionante progetto e per avermi insegnato ogni giorno un pezzettino nuovo di questo mestiere.

Ringrazio i miei genitori per essersi fidati di me ed avermi regalato l'opportunità unica di inseguire la mia passione.
Ringrazio mio papà per non avermi data per scontata, per aver dubitato all'inizio e per avermi dato la possibilità di dimostrare che cinque anni dopo (e non uno di più) alla fine "ce l'ho fatta".
Ringrazio mia mamma per ogni singola telefonata, per ogni "SOS lavatrice", per ogni prezioso consiglio, per ogni volta che in silenzio ha ascoltato e capito, per esserci sempre stata, vicina anche se lontana.

Ringrazio Flavio per aver creduto in me sin dall'inizio ben cinque anni fa, senza il quale "non avrei mai combinato un tubo" come dico sempre io.
Amore e collega da sempre, tu sai.

Ringrazio Gloria per il miglior team "le coinquiline", per le nostre serate padovane, per il Baileys, per le ore in palestra, per gli scleri e per le risate.

Ringrazio i miei ppatati, amici storici e fedeli da sempre.